https://doi.org/10.1016/j.cemconres.2021.106533

# AN INSIGHT ON THE EFFECT OF SODIUM AND SILICON ON MICROSTRUCTURE AND CRYSTALLOGRAPHY OF HIGH ALUMINA CEMENTS

M. CANTALUPPI
Earth Science Department "Ardito Desio", University of Milan, Via Botticelli 23, 20133, Milan, IT
marco.cantaluppi.it@gmail.com

N. MARINONI
Earth Science Department "Ardito Desio", University of Milan, Via Botticelli 23, 20133, Milan, IT
nicoletta.marinoni@unimi.it

F. CELLA
MAPEI S.p.A., R&D Central Laboratory, Via Carlo Cafiero 22, 20158, Milan, Italy
analysis.lab@mapei.it

A. BRAVO
MAPEI S.p.A., R&D Central Laboratory, Via Carlo Cafiero 22, 20158, Milan, Italy
a.bravo@mapei.it

F. CÁMARA
Earth Science Department "Ardito Desio", University of Milan, Via Botticelli 23, 20133, Milan, IT
fernando.camara@unimi.it

G. BORGHINI
Earth Science Department "Ardito Desio", University of Milan, Via Botticelli 23, 20133, Milan, IT
giulio.borghini@unimi.it

W. KAGAN
Gòrka Cement SP. Z. O. O., Lipcowa 58, 32540, Trezbinia, Poland
w.kagan@gorka.com.pl

**Abstract**

In the present study the influence of minor elements ($Na_2O$ and $SiO_2$) on the mineralogy, chemistry and microstructure of High Alumina Cements (HACs) has been investigated. HACs have several advantages respected to Ordinary Portland Cement (OPC) but the shortage of Al-rich raw materials represents a limiting factor: re-use of Al-rich waste as raw material represents a solution but it will add minor elements to the raw meal that could change HACs properties. For the first time, four commercial HACs, doped with sodium and silicon, and one synthetic HAC, only highly doped in sodium, were studied through a multidisciplinary approach by combining conventional and unconventional analytical techniques. Results highlighted that (i) sodium and silicon were mainly incorporated in a sodium-rich phase (*Na-phase*, $NCA_2$, $Na_{1.9}CaAl_{3.9}Si_{0.1}O_8$), (ii) no minor phases such as gehlenite and/or mayenite occurred, and (iii) CA ($CaAl_2O_4$) and $CA_2$ ($CaAl_4O_7$) revealed a limited ionic substitution.

***Keywords:*** X-Ray Diffraction; Calcium Aluminate Cement; Characterization; Synchrotron diffraction; Quantitative Rietveld Analysis

## 1. Introduction

Calcium Aluminate Cements represent an important type of cement significantly having many advantages respect to Ordinary Portland Cement (OPC), including early rapid hardening, enhanced durability properties, resistance to abrasion and alkali-silica reaction and sulphate attack, yet they are currently mainly used in refractory and building chemistry applications [1,2,3,4,5]. Three kinds of CACs are usually reported in literature and differ each other according to their chemical composition: i) standard CACs with low iron content (48-60% wt. $Al_2O_3$, < 3% wt. $Fe_2O_3$, 3-8% wt. $SiO_2$); ii) standard CACs with high iron content (36-42% wt. $Al_2O_3$, 12-20% wt. $Fe_2O_3$, 4-8% wt. $SiO_2$); iii) high alumina cements (HACs) (> 60% wt. $Al_2O_3$, < 1% wt. $Fe_2O_3$, < 0.5% wt. $SiO_2$) [1]. HACs represents the most important CACs for refractory castables and concrete with high early strength and sea water resistance, which is mostly based on high purity raw materials, such as pure limestone and high-quality synthetic alumina [6]. HACs is usually obtained by heating at 1500-1600 °C a mixture of bauxite and limestone [7], even though hydrated lime, laterite and different types of alumina can also be used as alternative raw materials [1]. The most common heating process involves the sintering of the raw meal at high temperature, followed by an air quenching [1].

Currently, the use of alternative raw materials with a wide range of chemical composition and origins (i.e. laterite, iron-rich bauxite, low grade alumina, blast furnace slags, Al-rich wastes, etc.) appears the most challenging frontier in CACs manufacture handling: (i) the shortage of bauxite deposits; (iii) the high energy demanding process of synthetic alumina production [8,9], which also requires to use several chemical compounds [20,73]; (iii) the dangerous wastes coming from aluminium industries, such as Al-anodizing waste [74], Al-slag (dross) [72,74] and gas cleaning dust from Al-electrolysis plants [74], which cause many ecological and healthy problems and have high treatment costs [71]. However, the alternative raw materials commonly introduce minor elements (i.e. manganese, titanium, copper, nickel, alkali elements and fluorine) and have a

different starting mineral assemblage (e.g. amorphous content in Al-rich metal slag) that can affect positively or adversely the cement manufacturing, as commonly observed in OPC [11,12,13,14,15.]. Several studies [10,16,17,18,19] studied the effects of minor starting from an appropriate mixture of analytical grade raw materials; the results prove that the final cement reactivity is hard to be predicted because it depends on the mutual interaction of the different ions/species. For example, silicon, which represents one of the most common impurities in limestone and in alumina, reduces the melting point and hydraulic properties by stabilizing of gehlenite ($C_2AS$, $Ca_2Al_2SiO_7$) during the CACs sintering.

The effects of minor elements that commonly appear as impurities in bauxite and limestone (i.e. iron, magnesium, nickel, silicon, manganese and titanium) on CACs have been broadly investigated whereas the role of alkaline elements and their mutual interaction is still matter of debate.

Despite the evidence of a broad range of sodium content (0.1-1% wt. $Na_2O$) in synthetic alumina, because of the Bayer process [20], and in different Al-rich wastes, such as aluminium dross (0.5-2.9% wt. $Na_2O$ [75]), Al-anodizing waste (0.3-8% wt. $Na_2O$ [71]), few studies have been carried out to understand its effects, and only on relatively simple chemical composition systems or at conditions far from HACs production. Ostrowski and Żelazny [21], and Verweij and Saris [22] studied in detail the alumina dominant system $CaO$-$Al_2O_3$-$Na_2O$, although they kept conditions studies below 1250 °C; Yu et al. [23] studied the effect of sodium on sintering of standard CACs at 1350 °C, revealing an increase in the stability field of mayenite ($C_{12}A_7$, $Ca_{12}Al_{14}O_{33}$) at the expense of gehlenite; Alex et al. [24] investigated the effect of adding sodium impurities on first heating of green, which highlighted the importance of limiting sodium content because of the formation of β-$Al_2O_3$ and the increase of linear thermal expansion.

Therefore, no effort was done to understand the role of sodium, both alone and combined with other common minor elements, on high-temperature sintering and the hydration of HACs, despite it is a very common impurity element.

In this light, a two-step approach is here considered to evaluate the influence of the simultaneous presence of sodium and silicon oxides on HACs cement: the content of dopants were below 2% wt. in order to reproduce common chemical condition on HACs manufacture. In the first step (*"Industrial HACs"* section), four HACs were prepared at industrial scale with different amounts of $Na_2O$ and similar $SiO_2$ and were investigated by means of a multidisciplinary approach. In particular, their mineralogy was characterised by both Laboratory and Synchrotron X-Ray Powder Diffraction (LXRPD, SXRPD) and Rietveld Quantitative Phase Analysis (RQPA). The distribution of the minor elements in the main phases was determined by an Electron Microprobe MicroAnalyser (EMPA) and Scanning Electron Microprobe (SEM) in back scattered mode (BSE) was used to investigate their microstructure on polished samples.

In the second step ("*Laboratory scale HACs*" section) the implication of high amount of $Na_2O$ (up to 3% wt.) on HACs manufacturing was investigated: Na-doped HAC cement was prepared at laboratory scale starting from an appropriate mixture of analytical grade raw materials which was further heated through a vertical high temperature furnace at 1550 °C for 1 h and then quenched to room temperature by pressurised air flux, trying to reproduce the same heating process of HACs manufacture. The stability fields of phase assemblages in the $CaO$-$Al_2O_3$-$SiO_2$ system, the temperature of liquid phase appearance and its composition as well as the achievement of its thermodynamic equilibrium were evaluated through a chemical-mineralogical characterisation of the obtained HAC cement. Moreover, the hydration process of a sodium-rich phase ($NCA_2$, $Na_2CaAl_4O_8$) synthetized at 1200 °C, which occurs in both Laboratory and Industrial HACs, was studied by LXRPD from 3 hours to 14 days, giving the first hydration data related to this crystal phase.

## 2. Sample preparation

*2.1. Industrial HACs*

In the first part of the present research, four different commercial HACs were prepared from a mixture of industrial-grade raw materials (decarbonated limestone at 950° C, high-grade and low-grade synthetic alumina) (Table 1) which was heated in a kiln feed at 1550±15° C for 1 h. In Fig. 1 the chemical composition range of industrial HACs is reported on the ternary phase diagram $CaO$-$Al_2O_3$-$SiO_2$ [1,2,3,4]. In Fig. 2 is reported the HACs manufacture heating process scheme: raw materials (limestone and bauxite) are quarried from the deposit and crushed; they are grinded and the bauxite is treated for producing synthetic alumina. The raw meal is obtained by mixing powders of limestone and synthetic alumina and is sintered in rotary kiln at temperature between 1550-1600 °C. This heating process is followed by a rapid quenching by an air stream and clinker nodules are grinded and stored in silos. Note that air quenching induces to a rapid cooling of the nodules which rapidly reach a temperature of 1100 °C [3]. The above-mentioned heating process is the same that occurs for Ordinary Portland Clinker manufacture, even though a higher temperature is reached in the rotary kiln.

The obtained samples are labelled as *HACx_y* where (i) *x* is *1* or *2* and refers to two HAC samples with different $CaO/Al_2O_3$ ratio and (ii) *y* is *LNa* or *HNa* and reflect the low and high sodium amount in the HACs samples, respectively. The chemical composition of the four investigated samples is reported in Table 2.

***Table 1****. Chemical composition obtained with XRF bulk analysis for raw materials used to prepare Industrial HACs. The esd were below 0.1% for all elements; *L.o.I = loss on ignition.*

| **Oxide** | ***Decarbonated Limestone* (% wt.)** | ***Synthethic Alumina High-Grade* (% wt.)** | ***Synthethic Alumina Low-Grade* (% wt.)** |
|---|---|---|---|
| $SiO_2$ | 1.61 | 0.04 | 0.06 |
| $Al_2O_3$ | 0.25 | 99.63 | 99.29 |
| $Fe_2O_3$ | 0.11 | 0.01 | 0.02 |
| CaO | 97.34 | <0.01 | <0.01 |
| $Na_2O$ | <0.01 | 0.21 | 0.55 |
| MgO | 0.13 | 0.01 | 0.01 |

| | | | |
|---|---|---|---|
| $SO_3$ | <0.01 | <0.01 | <0.01 |
| $K_2O$ | 0.04 | <0.01 | <0.01 |
| $P_2O_5$ | 0.10 | <0.01 | <0.01 |
| $Mn_2O_3$ | <0.01 | <0.01 | <0.01 |
| L.o.I* | 0.03 | 0.05 | 0.05 |
| Total | 99.97 | 99.95 | 99.98 |

***Table 2***. *Chemical composition of HACs obtained with XRF analysis. The esd were below 0.1% for all elements; *L.o.I = loss on ignition.*

| **Oxide** | ***HAC1_HNa* (% wt.)** | ***HAC1_LNa* (% wt.)** | ***HAC2_HNa* (% wt.)** | ***HAC2_LNa* (% wt.)** |
|---|---|---|---|---|
| $SiO_2$ | 0.37 | 0.50 | 0.41 | 0.44 |
| $Al_2O_3$ | 65.10 | 67.48 | 68.47 | 68.80 |
| $Fe_2O_3$ | 0.06 | 0.05 | 0.06 | 0.07 |
| CaO | 33.77 | 31.90 | 30.51 | 30.52 |
| $Na_2O$ | 0.62 | 0.10 | 0.55 | 0.11 |
| L.o.I.* | 0.05 | 0.03 | 0.04 | 0.05 |
| Total | 99.97 | 100.06 | 100.04 | 99.99 |

***Fig. 1.*** *Ternary phase diagram for $CaO$-$Al_2O_3$-$SiO_2$ [3]. The black bold type line represents the chemical composition range of industrial HACs analysed and the temperature is in Celsius degree.*

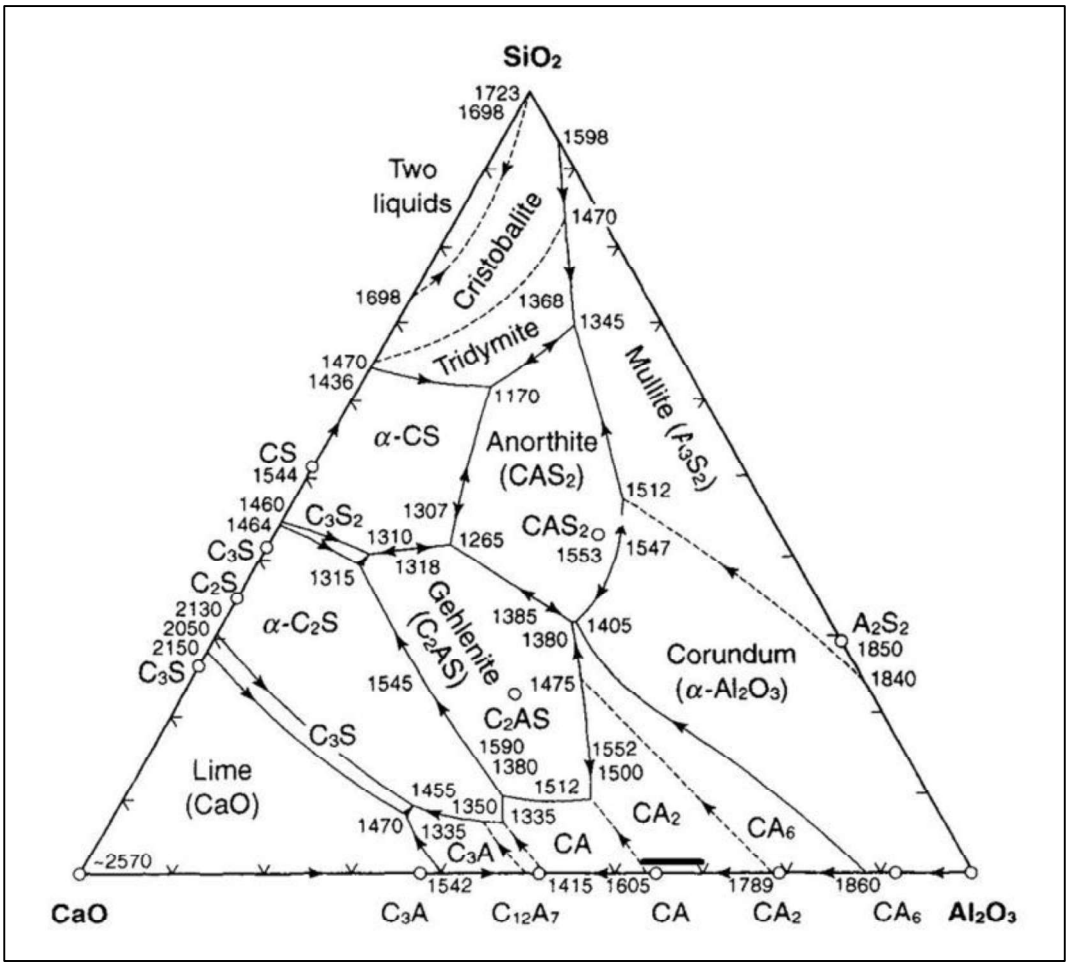


***Fig. 2.*** *Schematic representation of the heating process for HACs manufacture: the raw feed, which is commonly composed of a mixture of synthetic alumina and lime, is pre-heated and subsequently heated in a rotary kiln at 1550 °C. After firing, it is rapid cooled by air quenching, blended and grinded, as occurs for OPC manufacture plants.*

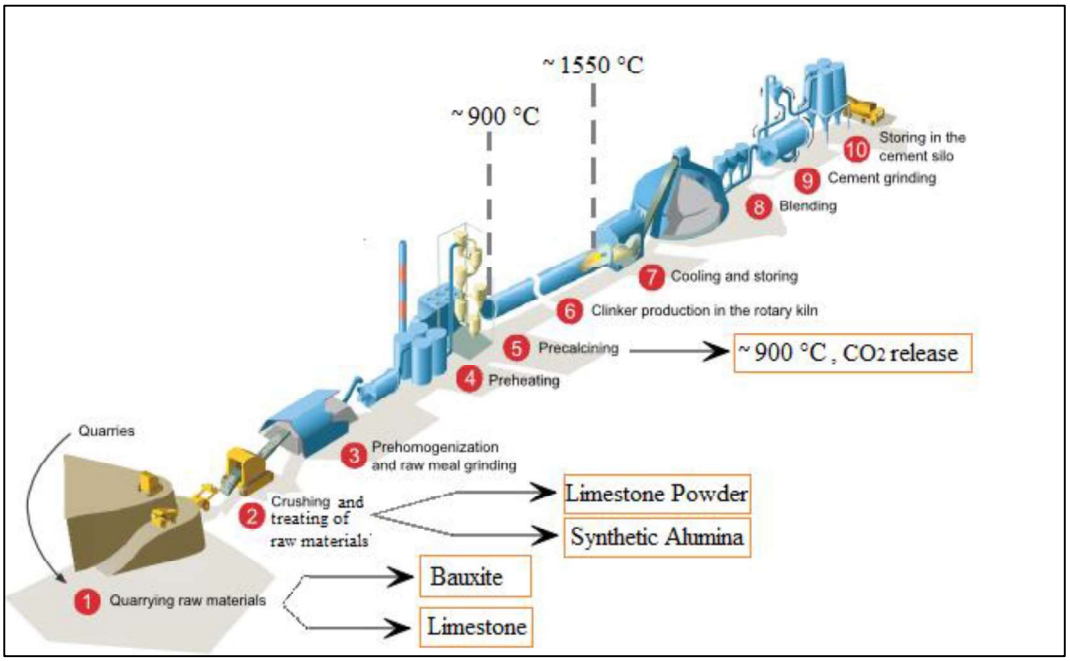

*2.2. Laboratory scale HACs*

In the second part of this research, to study the effects of high sodium content on HACs mineralogy and microstructure, the sample *Mix_CaNaAl* was prepared by mixing pure chemical reagents, such as sodium carbonate, calcium carbonate and alumina (Table 3). In particular, one pellet of about 2 g was prepared by using a double acting hydraulic press at 40 kN for 1 min, which was then heated at 1550±15° C for 1 h in a vertical furnace in a Pt capsule (Deltech Model DT-31VT-OS2). After heating, the pellet was extracted from the furnace and quenched using a pressured air jet. The chemical composition of these two sodium-rich mixes and the industrial HACs are reported on the liquidus projection of the $CaO$-$Al_2O_3$-$Na_2O$ ternary phase diagram [25] in Fig. 3. Fig. 3,5 were obtained from the open-access PhaseDiagram-Web source of FactSage v. 7.3, which uses the oxide database (FToxid) available at the Facility for the Analysis of Chemical Thermodynamics (FACT) at the Centre for Research in Computational Thermochemistry (CRCT) of the Ecole Polytechnique de Montreal and McGill University [25, 60].

Moreover, one sodium-rich mix (*Mix_NaP*) with the stoichiometric composition of $Na_2O{\cdot}CaO{\cdot}2Al_2O_3$ was prepared in order to synthethize the crystal phase $Na_2CaAl_4O_8$ (also reported as $NCA_2$ [21,22] or $N_2C_3A_5$ [34,35,37]), which occurred in both sodium-rich industrial and laboratory HACs, understanding the mineralogy, crystallography and hydration properties of this poorly studied crystal phase. By considering the isothermal section at 1200±15° C and 1 atm of the ternary phase diagram $CaO$-$Al_2O_3$-$Na_2O$ reported in Fig. 4, *Mix_NaP* plots exacltly on the $Na_2CaAl_4O_8$ crystal phase chemical composition (Table 2). The isothermal sections at 1200° C, obtained by Verweij and Saris from the numerous experimental data falling in the richer-$Al_2O_3$ portion (>50% wt. $Al_2O_3$) [22], is reported in Fig. 4. It is in good agreement with the same portion

of the isothermal section obtained from the open-access PhaseDiagram-Web source of FactSage v. 7.3 reported in Fig. 3.

*Mix_NaP* was prepared by mixing analytical grade raw materials, such as aluminium acetate hexahydrate, sodium carbonate and calcium carbonate in appropriated proportion Table 3. The mix was blended and ball milled for one hour with zirconia grinding media for appropriate particle intimacy. The milled materials were made into ≈ 10 g pellets in double acting hydraulic press at 50 kN for 60 sec. Pellets were heated in a furnace (Carbolite RHF 16/35 with SiC resistors) at 1200 °C for 24h in an open Pt crucible and finally quenched at room temperature with pressured air jet. After cooling, pellets were blended and ball milled in a zirconia grining media to obtain powders for subsequent XRD analysis. Pastes of *Mix_NaP* were prepared with a water cement ratio of 0.6, handly strirred for 2 min and then stored in a vessel at a constant temperature of 18 °C and with water saturation condition for the set times (3, 8 hours and 1, 7, 14 days) [1,3,70].

***Fig. 3.*** *Isothermal section of ternary phase diagram for CaO-$Al_2O_3$-$Na_2O$ at 1200° C obtained with FactSage and accessible from FactSage 7.3 database [25,60]; the green circle represents the chemical composition of Mix_NaP.*

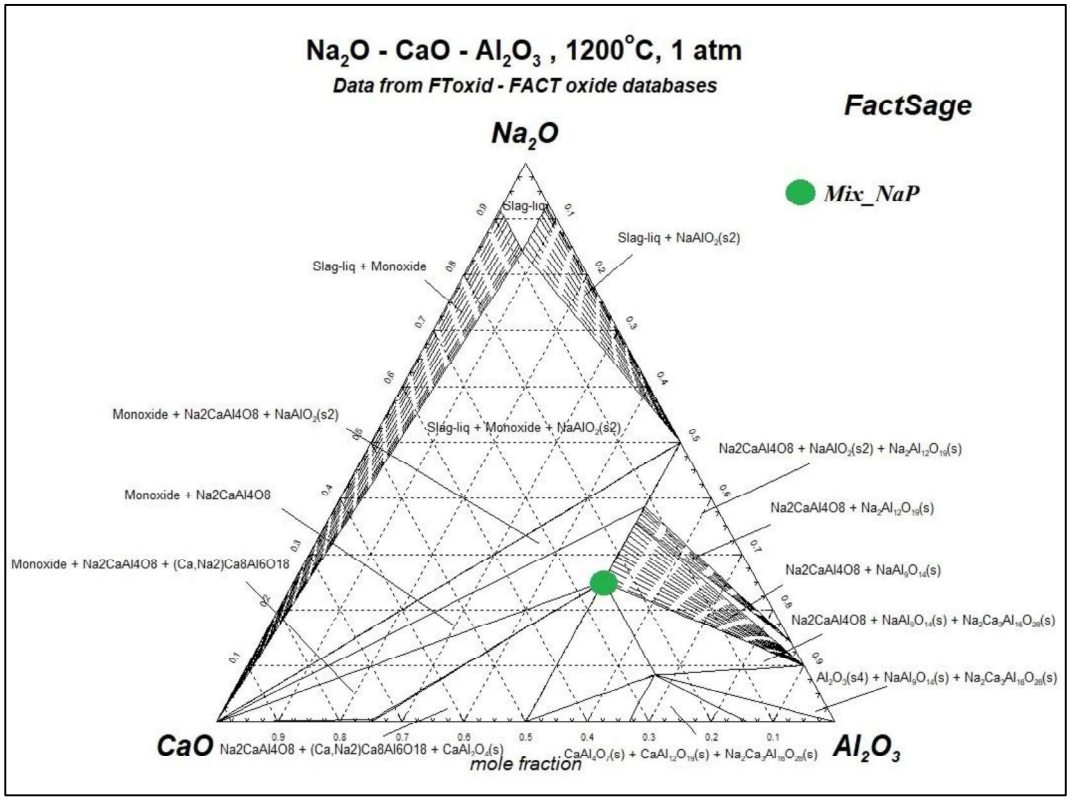

***Fig. 4.*** *Isothermal section of ternary phase diagram for $CaAl_2O_4$-$Al_2O_3$-$Na_2AlO_2$ at 1200 °C from Verweij and Saris, where each numbered point represents an experiment [22]; the green circle represents the chemical composition of Mix_NaP.*

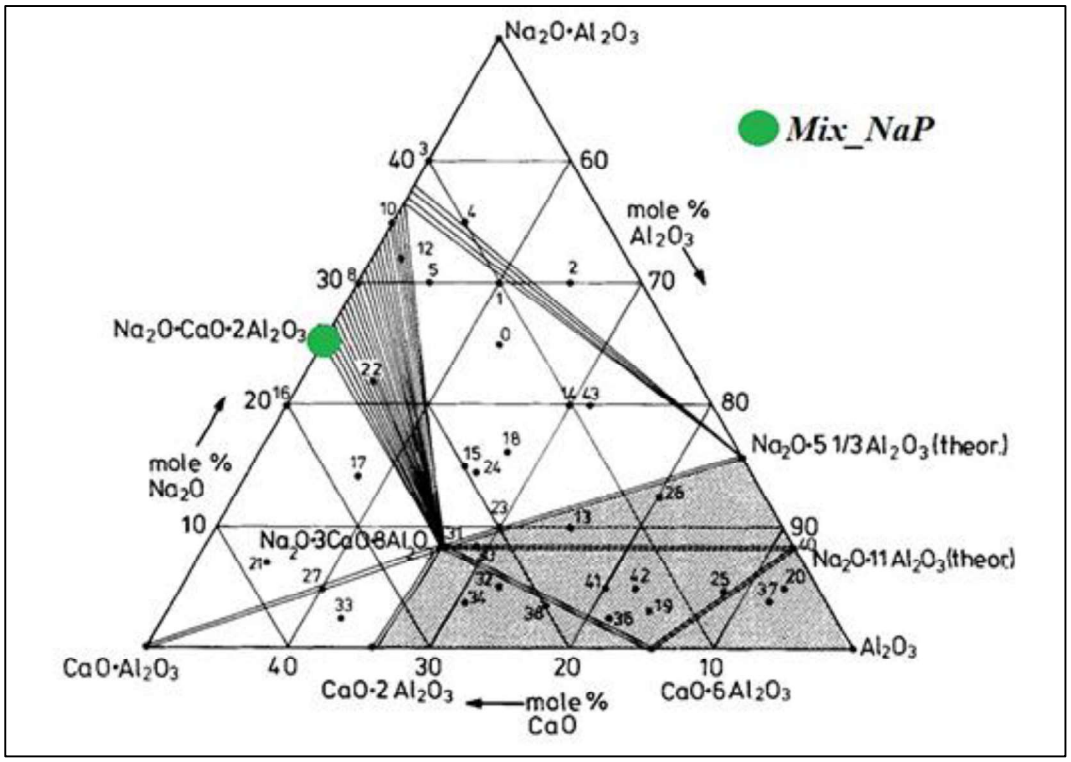


***Table 3.*** *Chemical composition of Mix_NaP and Mix_CaNaAl.*

| ***Mix*** | **$Al_2O_3$ (mol / % wt.)** | **$Na_2O$ (mol / % wt.)** | **CaO (mol / % wt.)** |
|---|---|---|---|
| *Mix_NaP* | 0.50 / 63.33 | 0.25 / 19.25 | 0.25 / 17.42 |
| *Mix_CaNaAl* | 0.54 / 67.92 | 0.04 / 3.08 | 0.42 / 29.00 |

***Fig. 5.*** *Liquidus projection (1 atm) of the ternary phase diagram for CaO-$Al_2O_3$-$Na_2O$ [25,60]. The temperature reported is in Celsius degree; blue and red circles represent the chemical composition of Mix_NaP and Mix_CaNaAl respectively, while the orange-thick line the covered chemical composition by industrial HACs.*

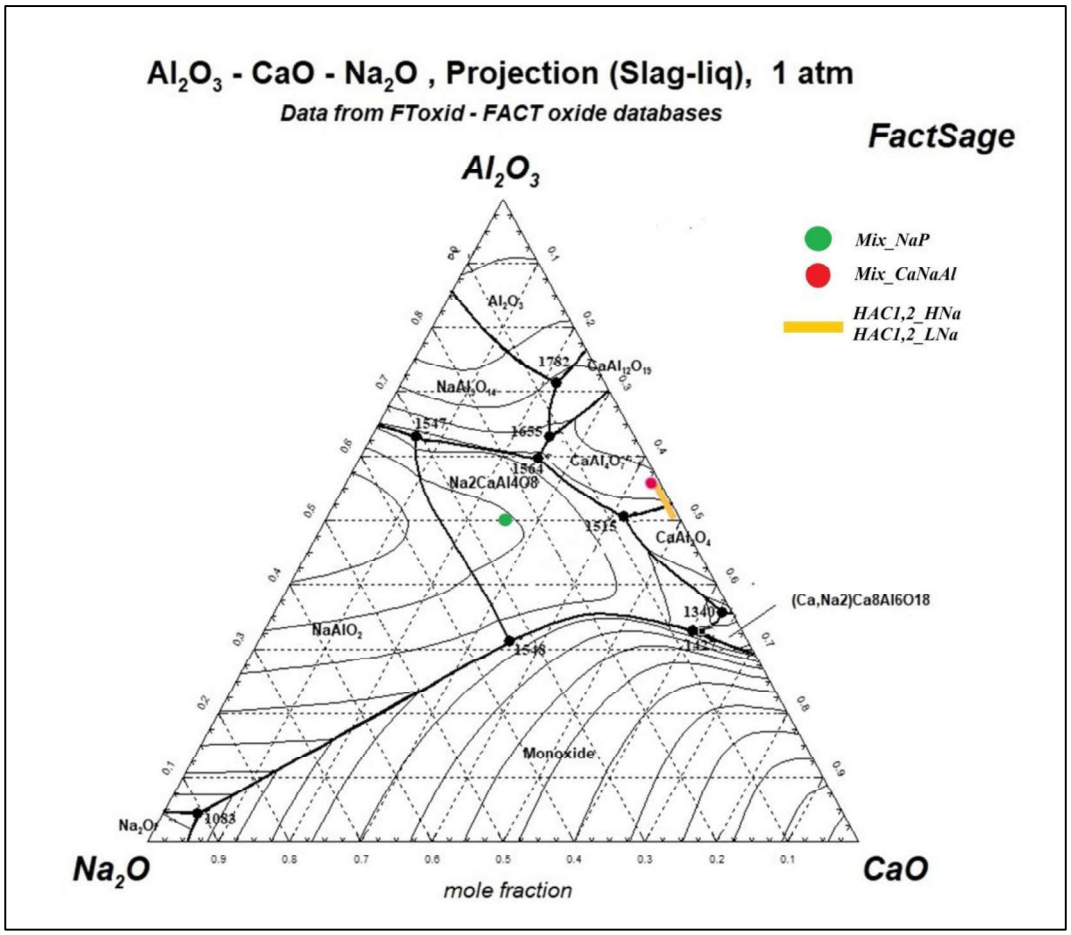


## 3. Experimental

### *3.1. X-Ray Fluorescence (XRF)*

The elemental composition of the starting raw materials and the final HAC's cements was measured through X-ray fluorescence (XRF) using a Bruker S8 Tiger WDXRF spectrometer with a Rh X-ray tube operating at 50 kv and 80 mA, and quantification was done by calibration of a group of 56 reference standards. The measure was carried out by using fused glass discs prepared by mixing 0.875 g of powdered whole samples with 6.125 g of lithium tetraborate lithium (corresponding to a 1:7 sample/borate dilution), carefully homogenized in a Pt (95%)-Au (3%)-Rh (2%) crucible, and heated for 15 min at 1000 °C. Fusion of the well-mixed flux and sample was performed on a Pt-Au-Rh crucible using a CLAISSE FLUXER-BIS! automatic apparatus. When the fusion was

completed, the melt was poured into a Pt-plate and slowly cooled. After cooling, the glass discs were used directly for analysis. Loss on ignition (L.o.I.) was determined gravimetrically by weighting the samples before and after a thermal treatment at T = 1000 °C for 45 mins.

*3.2. Laboratory X-Ray Powder Diffraction (LXRPD)*

LXRPD data acquisition was carried out by a X'Pert PRO Diffractometer (PANalytical), in θ-2θ Bragg-Brentano geometry, equipped with an X'Celerator LPS detector. The 1.54-9.00 *d* (Å) range has been investigated using Cu*K*α radiation for all industrial HACs (*HACx_HNa* and *HACx_LNa*), whereas the 1.20-17.00 *d* (Å) range has been investigated for all hydrated samples and *Mix_NaP*. All LXRPD analysis were performed with 40 kV current tension, 40 mA current intensity and 0.02° step size. The equivalent counting time was 60 s/step for all HACs samples both anhydrous and hydrated, whereas *Mix_CaNaAl* was analysed with 120 s/step; each analysis were performed with fixed divergence slits angle at 0.5°. Samples analysed with LXRPD were ground and then pressed in a back-load sample holder, excepted for *Mix_CaNaAl* and all hydrated samples of *Mix_NaP* which were analysed on a zero-background sample holder using ethanol as dispersion media.
In order to quantify the amount of amorphous phase content the internal standard method was applied on anhydrous industrial HACs, adding 10% wt. of Si powder (NIST 640d) [63,39,64. The amorphous fraction ($W_A$, % wt.) is obtained from the following equation [Eq. 1] [64], where *Ws* (% wt.) and $R_S$ (% wt.) represent the know amount of added internal crystalline standard and the Rietveld analysed concentration of the internal standard, respectively:

$$W_A = \frac{1}{100 - W_S}\left(1 - \frac{W_S}{R_S}\right) * 10^4 \qquad \text{Eq. 1}$$

The amorphous content includes not only the amorphous phase, which generally produce a hump in XRD pattern, but also all crystal phases which are not included in the Rietveld refinement method: a good amorphous evaluation requires to identify all crystal phases occurring in the powder.

Therefore, the "real" weight percent of each crystal phase ($W_\alpha$, % wt.) could be obtained by using the Rietvled analysed concentration for each crystal phase ($R_\alpha$, % wt.) and the amorphous content ($W_A$), as reported in the following equation [Eq. 2]:

$$W_\alpha = \frac{R_\alpha}{(\sum_{\alpha=1}^{n} R_\alpha)}(100 - W_A) \qquad \text{Eq. 2}$$

*3.3. Synchrotron X-Ray Powder Diffraction (SXRPD)*

SXRPD experiments were performed at beamline ID22 of the European Synchrotron Radiation Facility (Grenoble, FR) using a Debye-Scherrer configuration with a wavelength of λ = 0.35456 Å selected by a double-crystal Si (111) monochromator. Samples were loaded in borosilicate glass capillaries (diameter 2 mm) and rotated during data collection. The overall measuring time was 100 min in order to obtain very good statistics over the angular range 1.0-37.9° in 2θ, or over the distance range from 20 to 0.5 Å. The data from the monochromator Multi-Analyser Si (111) Stage coupled with the nine scintillation detectors were normalized and summed to 0.002° step size with local software to produce the final raw data [61,62].

The high-resolution nature of synchrotron data was meant to overcome the main drawbacks of the laboratory XRPD experimental set up, such as strong peak overlapping, absorption, peak broadening and preferred orientation, thus allowing to detect minor phases as well as to obtain a more accurate quantitative phase analysis.

*3.4. Rietveld Quantitative Phase Analysis (RQPA)*

LXRPD and SXRPD profiles were fitted using the software TOPAS-Academic v.4.6, which is based on the Rietveld method and Full Parameter Approach [26,27,28]. Rietveld refinement was applied over the entire measured profile refining cell parameters, crystallite size, individual scale

factor, zero shift and using a Chebychev polynomial function with four terms for describing the background function for all anhydrous samples, whereas a polynomial function with 15 terms was used for all hydrated samples.

Crystal structural models used in this work during Rietveld Quantitative Phase Analysis are listed below: CA ($CaAl_2O_4$) [29]; $CA_2$ ($CaAl_4O_7$) [30]; Si [47,50]. All the reported crystal structure model were found using the open-access Crystal Open Database (COD) [52,53,54,55,56,57].

*3.5. Scanning Electron Microprobe (SEM) and Electron MicroProbe Analysis (EMPA)*

Pellets of the investigated samples were embedded in epoxide resin. Dry-out polishing conditions were applied using abrasive papers with decreasing grain size and finished with diamond paste (1 μm). An ultrasonic bath in hexane was carried out between every abrasive paper change to remove the residual powder derived from the previous polishing. Samples were covered with a sputtered graphite layer to ensure conductivity. Quantitative chemical analyses were performed on resin embedded samples using a JEOL JXA-8200 Electron MicroProbe Analyser in Wavelength-Dispersive mode, with an accelerating voltage of 15 kV, an electron probe spot size of 1μm, a beam current of 10 nA, a counting times of 30 s on peaks and 10 s on backgrounds. The following elements were measured: Si, Al, Ca, Fe, K, Mg and Na. Natural kyanite ($Al_2SiO_5$, for Al, Si, TAP Kα-lines ), anorthite ($CaAl_2Si_2O_8$, for Ca. PET Kα-line), fayalite ($Fe_2SiO_4$, for Fe, LIF Kα-line), K-feldspar ($KAlSi_3O_8$, for K, PET Kα-line) and olivine ($(Mg,Fe)_2SiO_4$, for Mg, TAP Kα-line), omphacite ($(Na,Ca)(AlMg)Si_2O_6$, for Na TAP Kα-line) have been employed as standards. Raw data were corrected for matrix effects using a conventional ΦρZ routine in the JEOL soft-ware package [31].

These polished sections were also investigated by means of a Zeiss EVO MA15 Scanning Electron Microscope operating with an acceleration current of 15 kV, a beam size of 100 nm and a working

distance of 11 mm, with an image resolution of 1024 x 730 pixels. Microstructural analysis was performed using detection of BackScattered Electrons (BSE).

## 4. Results

### *4.1. Industrial HACs*

The samples reported in Table 2 were studied. Comparison with a sample mimicking industrial HACs doped with high-amount of $Na_2O$ (*Mix_CaNaAl* Table 3) is also reported and discussed. First of all, the sensibility of the two diffractometric approaches are discussed. In Fig. 6a comparison between the XRPD patterns of *HAC1_HNa* collected with a Laboratory source and Synchrotron radiation is reported by way of example. It is evident that the two patterns provide comparable information, showing that the industrial samples consist of a mixture of CA and $CA_2$. No evidences of minor crystallite phases commonly found in HACs, such as gehlenite (ICDD 35-0755), brownmillerite (ICDD 42-1469), mayenite (ICDD 09-0413), hibonite (ICDD 38-0469) and alumina (ICDD 10-0173) were detected. An unresolved peak with low intensity and wide peak broadening occurs at 4.22 Å but only in the SXRPD pattern (see the inset of Fig. 6). It should be attributed to an unknown minor crystal phase which is described in the next paragraphs.
Structural refinement during Rietveld analysis did not highlight significant variations in the cell parameters of the two aluminate phases (Supplementaray Materials Table 1). From the analysis of the QXRPD data reported in Table 4 three main results can be drawn: (i) $Na_2O$ and $SiO_2$ doping do not affect the main phase contents by comparing *HAC1_HNa* and *HAC1_LNa* Rietveld results; (ii) large differences in phase assemblage can be observed between the samples *HAC2_y* and *HAC1_y* (i.e. CA ranges from 78% to 55% wt. in *HAC1_HNa* and *HAC2_HNa*, respectively), despite the close chemical composition of their starting raw meals (Table 2); (iii) discrepancies in the amount

of crystalline phases detected by LXRPD and SXRPD results are not explained by their estimated standard deviation. This latter evidence can be attributed to the fact that the SXRPD collects data over a greater *d*-spacing range allowing a larger degree of freedom [32,33] and thus leading to more accurate QXRPD results. Therefore, the crystalline phases content is better represented by SXRPD Rietveld data than LXRPD one. The evaluation of the amorphous content (% wt.) on anhydrous HACs by the internal standard method with laboratory condition highlighted that all sodium-rich HACs (*HACx_HNa*) have a mean of 3.5% wt. of amorphous content that is about twice respected to all sodium-depleted HACs (*HACsx_LNa*). In Fig 7 is reported the LXRPD of *HAC1_HNa* with the internal standard. Consequently, the "real" relative abundance (% wt.) of CA and $CA_2$ does not change significalty by the occurrence of an amorphous content in all HACs samples (Table 4).

A different approach for modal quantification of phases in HACs is based on SEM investigations, which confirm the differences in terms of phase contents observed by diffraction. From a microscopical point of view, all the samples exhibit a similar microstructure. However, it is observed a different modal distribution of the aluminate phases. In particular, in all the industrial HACs samples, tabular to sub-rounded $CA_2$ crystals with a size ranging from 40 to 100 μm are intimately associated to form clusters up to 500 μm in length. On the contrary, CA is xenomorphic and does not exhibit a regular shape (Fig. 8).

Moreover, a detailed inspection of BSE images highlighted the occurrence of an unknown phase, hereafter called as *Na-phase*, which can be easily detected in the images because of its lower BSE grayscale values than the ones associated to CA and $CA_2$ (Fig. 8). This phase exhibits an anhedral shape with a size up to 10 μm in length and appears always embedded in clusters of $CA_2$ crystals. Note that this phase is widespread within the $CA_2$ clusters in *HACx_HNa* samples (Fig. 8a,b) whereas it exhibits a more limited distribution in the *HACx_LNa* ones (Fig. 6c,d). This interstitial unknown phase seems to be highly correlated to the appearance of the unresolved peak in SXRPD patterns (see by instance the inset in Fig. 6a).

Using the different BSE contrast a 2D-estimation of the modal abundances of CA, $CA_2$ and *Na-phase* can be obtained. This has been done by means of Image Analysis using ImagePro Plus v. 4.5. Two snapshots are shown in Fig. 9a,b and the differences in modal distribution obtained by this analysis are highlighted in Table 5 , confirming an higher content of *Na-phase* for sodium rich HACs.

Quantitative chemical analyses obtained with the microprobe allowed to obtain a chemical characterisation of phase occurence in HACs samples (Supplementary Materials Table 2). Three main evidences are observed: (i) CA and $CA_2$ have always a chemical composition close to a pure crystal phase; (ii) CA has an average content of 0.16% wt. $Na_2O$ and 0.3% wt. $SiO_2$, which is twice and one higher order of magnitude than $CA_2$, respectively; (iii) no differences in the minor element contents, such as $Fe_2O_3$, MgO and $K_2O$, between the two calcium aluminate occurred, as expected from the low-content of these elements in the raw meals. Despite the low and limited content of $Na_2O$ and $SiO_2$ in CA crystals, a clear negative correlation between the Ca+Al (apfu) *vs* Na+Si (apfu) for CA crystals can be traced using EMPA results of sodium-rich HACs (Fig. 9): a coupled heterovalent substitution involving $Na^+$ and $Si^{4+}$ replacing $Ca^{2+}$ and $Al^{3+}$, respectively.

The chemical composition of the *Na-phase* among HACs samples was obtained as an average on 10 points analyses for each samples. It consists mainly of sodium, aluminium, calcium oxides and minor amounts of $SiO_2$, with an average empirical formula of $Na_{1.9}CaAl_{3.9}Si_{0.1}O_8$ in sodium-rich HACs that could be reported in the cement nomenclature as $NCA_2$, excluding $SiO_2$ content. The occurrence of $SiO_2$ should be related to an heterovalent substitution of $Al^{3+}$ by $Si^{4+}$ which could be compensated mainly by coupled substitution between $Ca^{2+}$ and $Na^+$ ($Al^{3+} + Ca^{2+} \leftrightarrow Si^{4+} + Na^+$ ), as observed of CA crystals. Minor amounts (< 0.02 apfu) of $Mg^{2+}$ and $K^+$ occurred in the *Na-phase* in *Mix_CaNaAl*, probably replacing $Ca^{2+}$ and $Na^+$, respectively. The average empirical formula obtained is similar to the observed one for $NCA_2$ by Sengo et al. [65] ($Na_{1.97}Ca_{0.94}Al_{3.86}Si_{0.14}$) in metal-slags, which the latter commonly contains much more impurity respect to the stoichiometric compound.

*Na-phase* revealed an average empirical formula of $Na_{1.8}Ca_{1.1}Al_4O_8$ in *Mix_CaNaAl*, which is silicon free respect to industrial HACs: this chemical composition falls withing the range between the $Na_2CaAl_4O_8$ ($NCA_2$) crystal phase of Verweij and Saris [22] and the $Na_{1.6}Ca_{1.2}Al_4O_8$ ($N_2C_3A_5$, $3CaO{\cdot}2Na_2O{\cdot}5Al_2O_3$) reported by Brownmiller and Bogue [34], Ostrowski and Żelazny [21] and Tian et al. [35]. Therefore, on the basis of these chemical evidences a small amount of $Na^+$ could be replaced by half-amount of $Ca^{2+}$ and $Na^+$ vacancies ($Ca^{2+} + \square \leftrightarrow 2\ Na^+$), maintaining the charge balance.

The comparison between the XRF observed values and the chemical composition, calculated by combining chemical results from EMPA analysis and RQPA corrected from the internal standard method (Table 3) only for two sodium-rich industrial HACs, is reported in Table 6: $Na_2O$, CaO, $SiO_2$ and $Fe_2O_3$ contents are always underestimated by XRF calculated respect to the observed one (Table 2). The difference in the amorphous content between sodium-rich and sodium-depled HACs (Table 4) is around 2.1% wt. and seems to be related only to the occurrence of the *Na-phase*: the calculated amount of *Na-phase*, which was obtained from the aforementioned underestimation of $Na_2O$ and EMPA data, is about 2% wt. for both sodium-rich HACs.

***Fig. 6.*** *Patterns for HAC1_HNa: a) at large scale facility; b) at laboratory scale. Principal peaks for CA (ICDD 70-0134), $CA_2$ (ICDD 23-1037) and Na-phase ($Na_2CaAl_4O_8$) are reported as filled black triangles, filled black diamond and black filled star, respectively. A detailed inspection for the angular range 4.1-4.5 Å is reported in the inset, highlighting occurrence of the unresolved peak observed only for SXRPD pattern.*

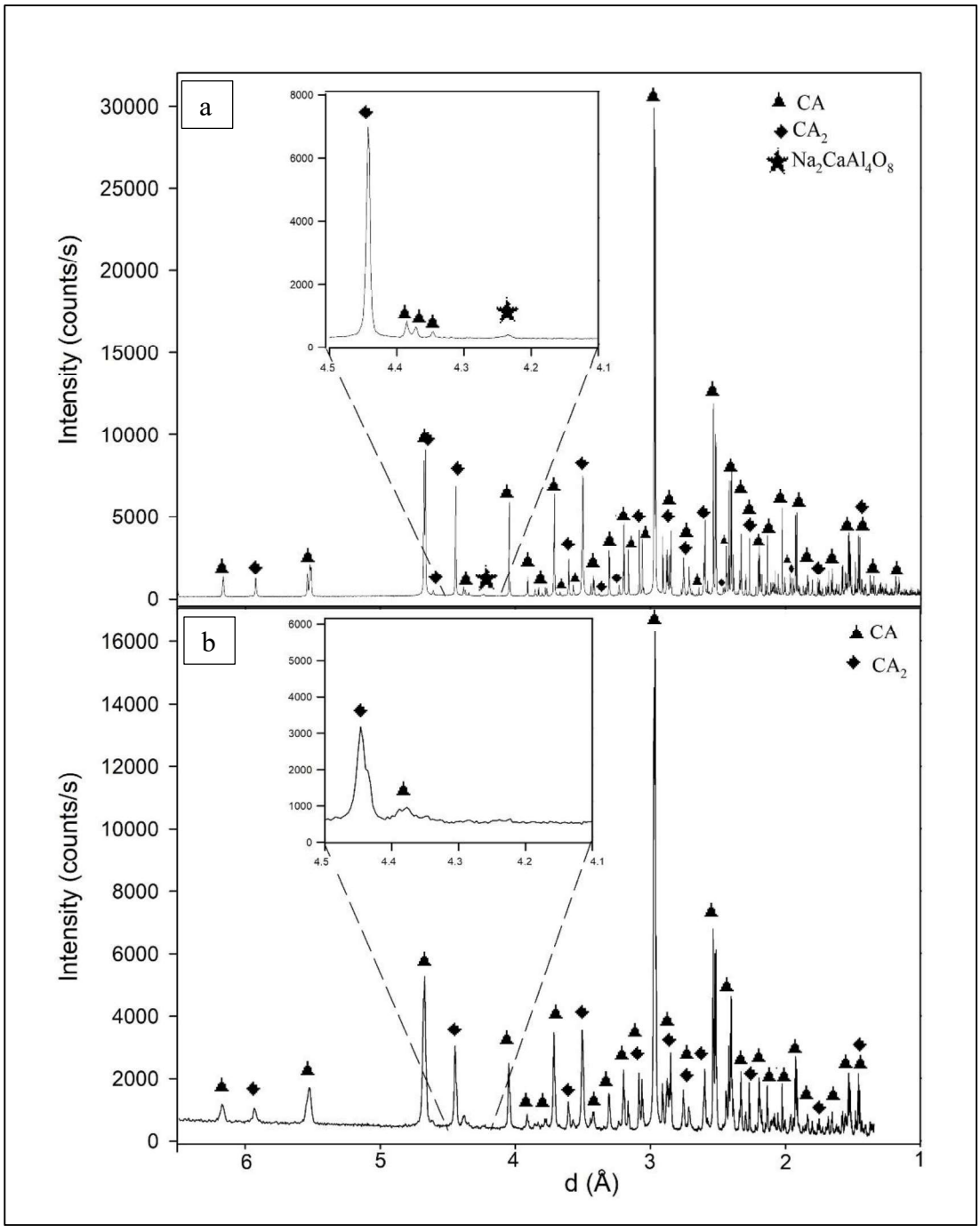
a
b
CA
CA2
Na2CaAl4O8
Intensity (counts/s)
d (Å)

***Fig. 7.*** *Patterns for HAC1_HNa+SiNist at LXRPD: Principal peaks for CA (ICDD 70-0134), $CA_2$ (ICDD 23-1037) and Silicon Standard are reported as filled black triangles, filled black diamond and empty hexagon, respectively.*

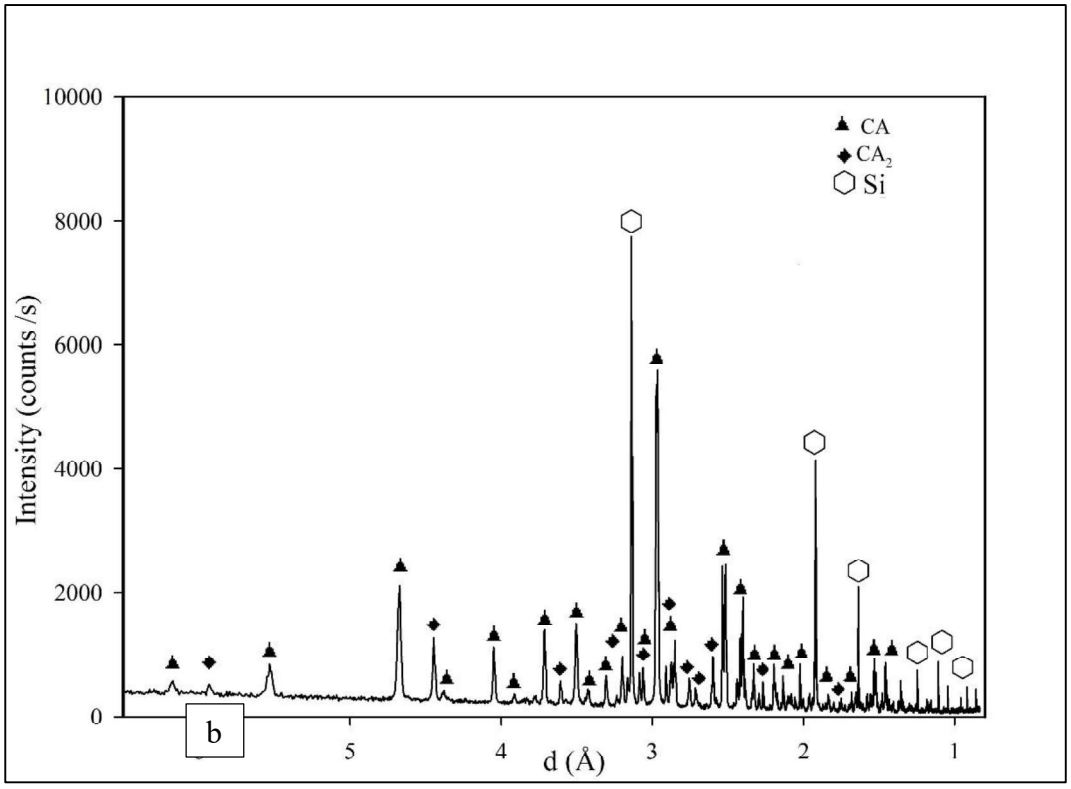

***Table 4.*** *Results from QXRPD for all HACs samples; e.s.d in brackets; * Rietveld refinement was carried out without including the Na-phase, despite its evidence.*

| ***ANHYDROUS HACs*** | **Type** | **CA (% wt.)** | **$CA_2$ (% wt.)** | **Amorphous Phase (% wt.)** | **$R_{exp}$** | **$R_p$** | **$R_{wp}$** | **GoF** |
|---|---|---|---|---|---|---|---|---|
| ***HAC1_HNa*** | **LXRPD** | 78.7(3) | 21.3(4) | - | 3.82(5) | 7.59(5) | 9.58(6) | 2.50(5) |
| | **SXRPD** | 77.6(2) | 22.4(1) | - | 4.91(2) | 8.30(2) | 11.16(4) | 2.27(3) |
| | **LXRDP+STD** | 76.0(3) | 20.7(3) | 3.3(9) | 6.83(7) | 9.89(3) | 12.30(5) | 1.80(3) |
| ***HAC1_LNa*** | **LXRPD** | 79.3(4) | 20.7(4) | - | 4.13(5) | 5.95(6) | 7.48(3) | 1.80(5) |
| | **LXRDP+STD** | 78.0(3) | 20.3(2) | 1.7(7) | 6.83(6) | 8.09(4) | 10.11(7) | 1.48(5) |
| ***HAC2_HNa*** | **LXRPD** | 56.1(3) | 43.9(4) | - | 3.76(6) | 7.30(5) | 9.27(4) | 2.46(8) |
| | **SXRPD** | 55.1(2) | 44.9(2) | - | 4.83(3) | 8.05(2) | 10.82(3) | 2.23(3) |
| | **LXRPD+STD** | 53.3(3) | 42.8(3) | 3.9(6) | 6.76(4) | 9.07(3) | 11.42(5) | 1.69(6) |
| ***HAC2_LNa*** | **LXRPD** | 57.7(3) | 42.3(4) | - | 4.20(3) | 6.27(6) | 8.47(5) | 2.01(5) |
| | **LXRPD+STD** | 56.8(2) | 42.7(3) | 1.5(6) | 6.71(4) | 8.69(6) | 10.94(3) | 1.63(5) |
| ***MIX_CaNaAl**** | **LXRPD** | 67.29(4) | 32.71(4) | - | 4.02(5) | 13.12(6) | 19.26(7) | 4.78(5) |

**Fig. 8.** *BSE images: a) a detail of HAC2_HNa, which highlights features of Na-bearing phase and* $CA_2$ crystals; *b) an overview at lower magnification of HAC1_HNa, which highlights features of* $CA_2$ *clusters; c) a detail of sample HAC2_LNa, which highlight the scarcity of Na-bearing phase; d) an overview at lower magnification of HAC1_LNa. In the images: light-grey CA, medium-grey* $CA_2$*, dark-grey Na-phase and black void.*

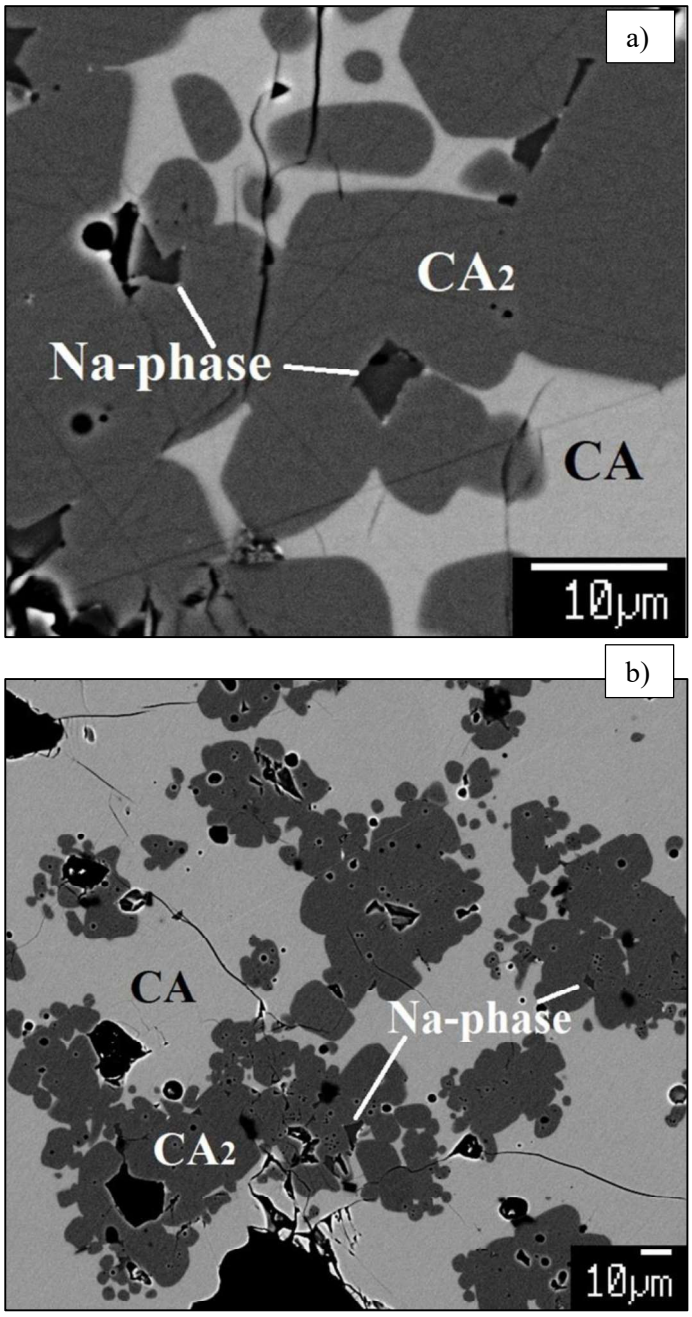

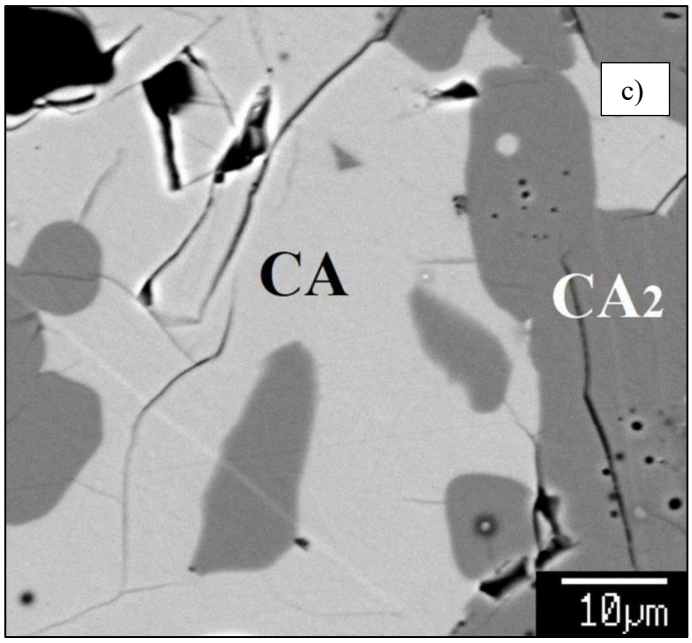
c)
CA
CA2
10µm

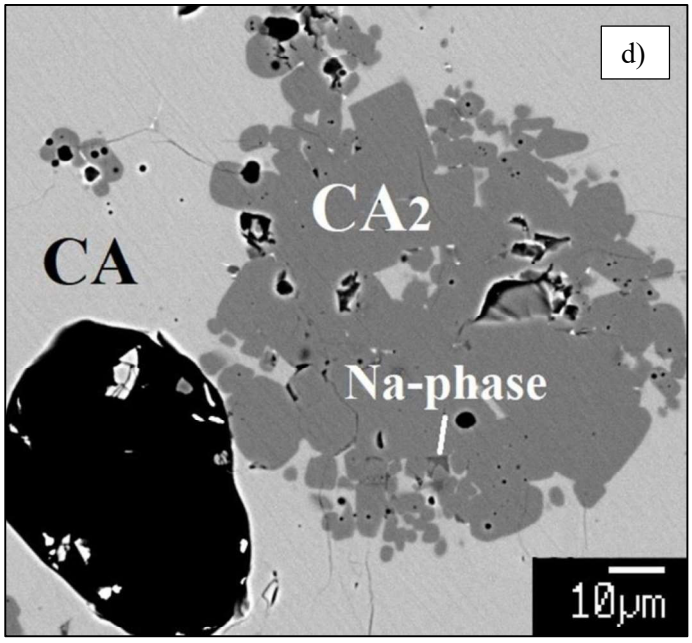
d)
CA2
CA
Na-phase
10µm

**Fig. 9.** *Image Analysis of two industrial HACs: a) HAC1_HNa; b) HAC1_LNa. Red colour represents CA, yellow $CA_2$, blue Na-bearing phase and black voids.*

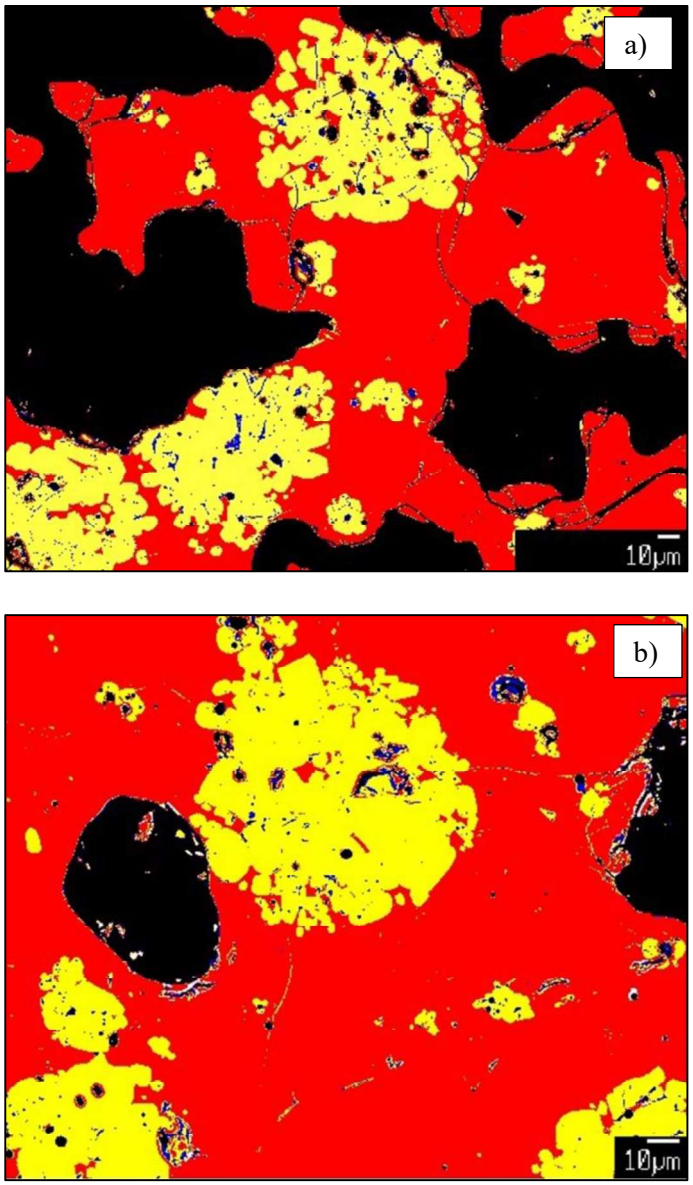


***Table 5.*** *Results from Image Analysis (% vol.) for two industrial HACs and the laboratory one.*

| | ***HAC1_HNa*** | ***HAC1_LNa*** | ***Mix_CaNaAl*** |
|---|---|---|---|
| **CA** | 67.99 | 72.02 | 61.11 |
| **$CA_2$** | 30.10 | 26.56 | 27.15 |
| **Na-phase** | 1.90 | 1.42 | 11.74 |
| **Total** | 100 | 100 | 100 |

***Fig. 10.*** *Ca+Al (apfu) vs Na+Si (apfu) in CA crystals from both HAC1_HNa and HAC2_HNa.*

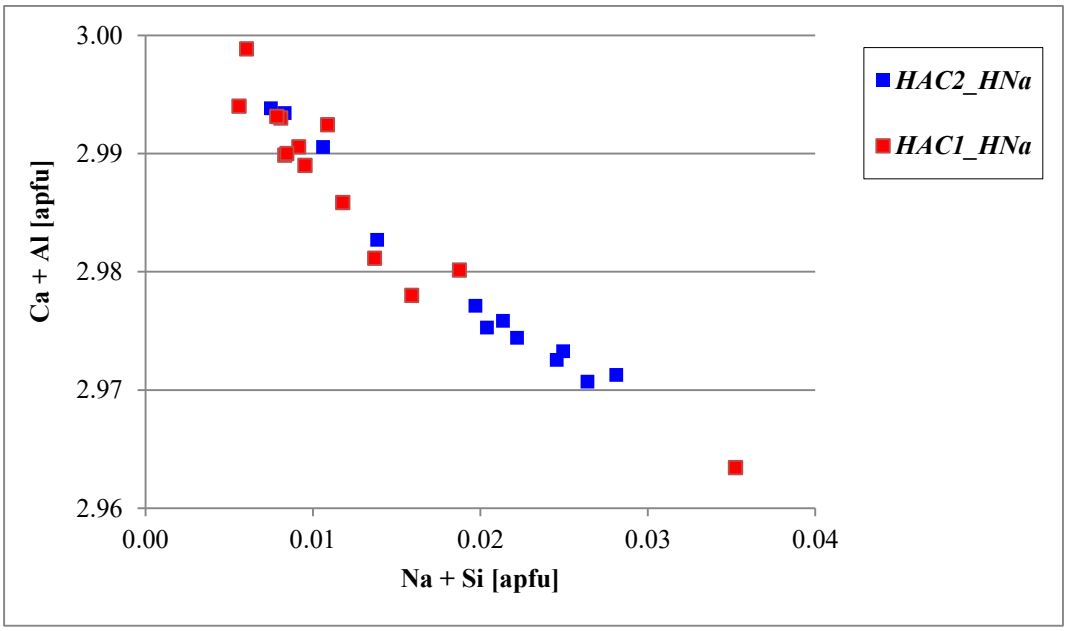


***Table 6.*** *XRF calculated using RQPA corrected from amorphous content and EMPA data for two rich sodium industrial HACs. Δ represents the difference between XRF observed (see Table 1) vs calculated.*

| Oxide | *HAC1_HNa* (% wt.) | Δ (% wt.) | *HAC2_HNa* (% wt.) | Δ (% wt.) |
|---|---|---|---|---|
| **CaO** | 31.57 | 2.20 | 28.31 | 2.19 |
| **$Na_2O$** | 0.14 | 0.48 | 0.15 | 0.36 |
| **$SiO_2$** | 0.16 | 0.21 | 0.19 | 0.23 |
| **$Fe_2O_3$** | 0.03 | 0.04 | 0.02 | 0.05 |
| **$Al_2O_3$** | 65.62 | -0.52 | 68.45 | 0.02 |
| **Total** | 97.52 | 2.41 | 97.11 | 2.86 |

## *4.2. Laboratory scale HACs*

In order to study the *Na-phase* ($NCA_2$, $Na_2CaAl_4O_8$) occurring in all sodium-rich industrial HACs, one stoichiometric raw meal (*Mix_NaP*) was prepared and heated at 1200±15° C for 24 hours (Table 3); whereas *Mix_CaNaAl* represents a highly sodium doped HAC ( ~3% wt. $Na_2O$), giving the chance to understand the effects of very high sodium content on HACs microstructure and crystal phase assemblage.

In Fig. 11 a comparison between the XRPD patterns of *Mix_NaP* and *Mix_CaNaAl* is reported: *Mix_CaNaAl* is composed of mainly CA ($CaAl_2O_4$, ICDD 70-0134) and $CA_2$ ($CaAl_4O_7$, ICDD 33-

1200), but many Bragg peaks remain unresolved; *Mix_NaP* has almost all Bragg peaks in the same *d* (Å) positions of those one unresolved in *Mix_CaNaAl*. The aforementioned unresolved Bragg peaks are in extreme good agreement with Bragg peaks reported for $NCA_2$ by Verweij and Saris [22], and $N_2C_3A_5$ by Tian et al. [35], Brownmiller and Bogue [34] and Yu et al. [43]: $NCA_2$ and $N_2C_3A_5$ represent the same crystal phase (in this work called *Na-phase*) but with changes in chemical composition. Therefore, *Mix_CaNaAl* and *Mix_NaP* are both composed of *Na-phase*, but in the former samples represents a minor crystal phase, whereas in the latter the main one (Fig. 11). The lack of information of a crystal structure model for *Na-phase* ($NCA_2$ or $N_2C_3A_5$) does not allow a quantitative phase analysis of laboratory samples (*Mix_NaP* and *Mix_CaNaAl*) by Rietveld method. The indexing of unresolved peaks and space group resolving were performed by means of GSAS II [41,68] and EXPO [49] softwares using auto-indexing functions: the unresolved peaks attributable to $Na_2CaAl_4O_8$ on *Mix_CaNaAl* pattern are compatible with an orthorombic crystal system with $P2_12_12_1$ space group and $a$ = 7.2510 Å, $b$ = 10.4304 Å and $c$ = 10.4348 Å cell parameters. A detailed inspection of *Mix_NaP* pattern revealed the occurrence of minor amount of $CA_2$ and Bragg peaks that fit with $NC_3A_8$ ($Na_2Ca_3Al_{16}O_{28}$), which has an exagonal crystal structure ($a = b$ = 9.8436 Å and $c$ = 6.9415 Å) [22]. No NA ($NaAlO_2$, ICDD 33-1200) where detected despite many authors reported the decomposition of *Na-Phase* during cooling from high-temperature due to a solubility gap between these sodium-rich crystal phases [22,34].

SEM investigations confirmed a whole textural similarity between industrial HACs and *Mix_CaNaAl* even though slight differences appear in the crystal phase habit. In particular, in the *Mix_CaNaAl* tabular $CA_2$ crystals occurred arranged in clusters as well as the *Na-pha*se, which was usually observed as prismatic crystals with a size up to 20 μm which grow within the $CA_2$ clusters (Fig. 10a). Furthermore, image analysis on SEM images revealed a higher areal distribution of *Na-phase* in *Mix_CaNaAl* when compared to industrial HACs (Fig. 12b and Table 5).

The WDS-EMPA analysis on *Mix_CaNaAl* (Supplementary Materials Table 2) highlighted a similar chemical composition of CA and $CA_2$ that had the same amount of sodium content respect

to commercial HACs. The lack of $SiO_2$ content among crystal phases in *Mix_CaNaAl* should related to its lack in the starting raw materials. *Na-phase* revealed a slight increase in CaO and a decrease in $Na_2O$ content in *Mix_CaNaAl* respect to industrial HACs:

***Fig. 11.*** *Diffraction patterns at laboratory scale for: a) Mix_NaP; b) Mix_CaNaAl. Principal peaks for CA, $CA_2$, $Na_2CaAl_4O_8$ and $Na_2Ca_3Al_{16}O_{28}$ as black filled star, circle, triangle and diamond, respectively. In short dotted lines are highlighted principal peaks of $Na_2CaAl_4O_8$ present in both XRD patterns.*

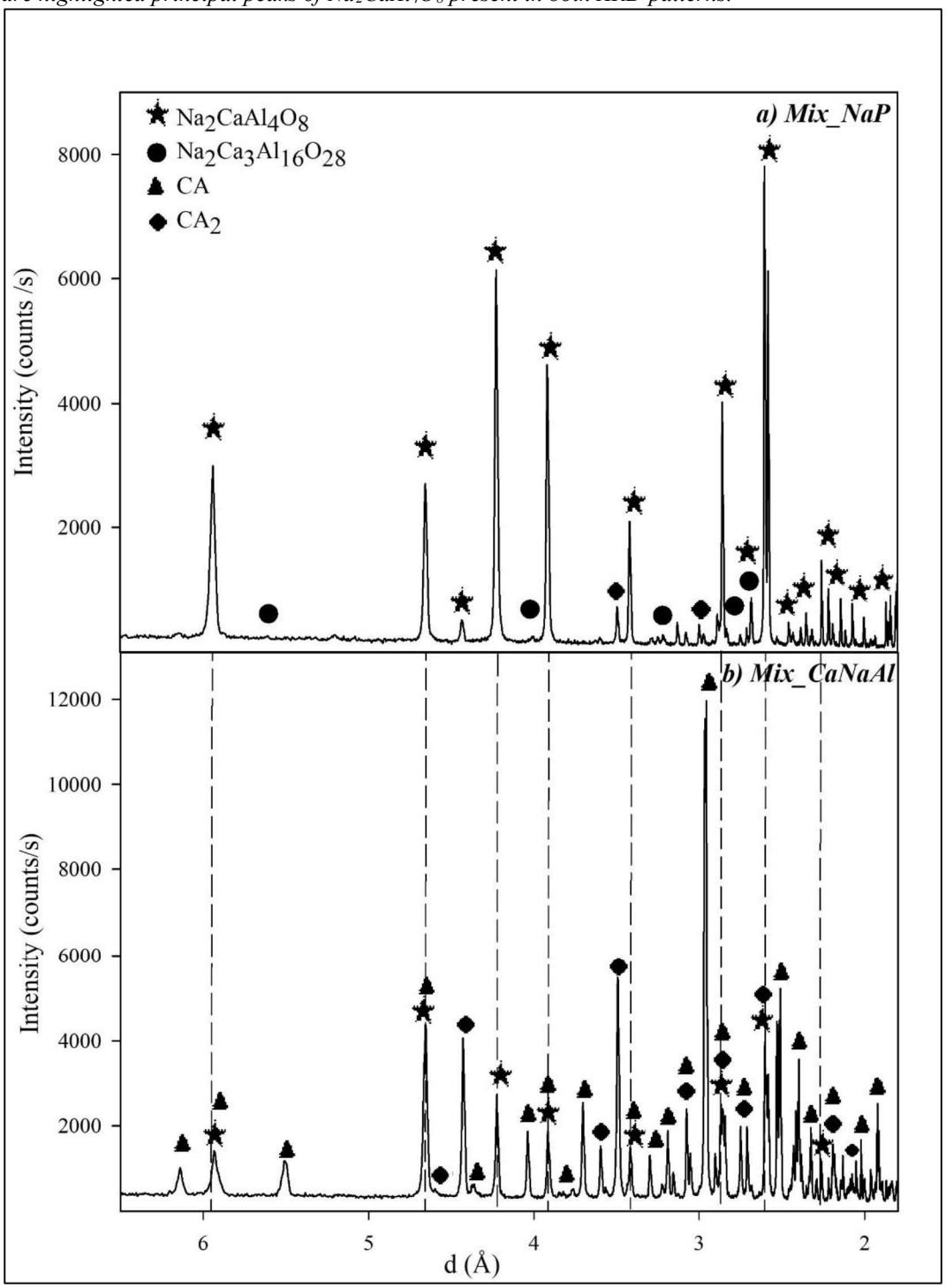

**Fig. 12.** *BSE images of Mix_CaNaAl at medium magnification: a) BSE image highlighting shape and distribution of crystals, with light-grey, medium-grey and dark-grey colour CA, $CA_2$ and Na-phase, respectively; b) processed image by Image Analysis of the area within the white dotted rectangle in a), in red colour, yellow, blue and black colours are CA, $CA_2$, Na-phase and voids, respectively.*

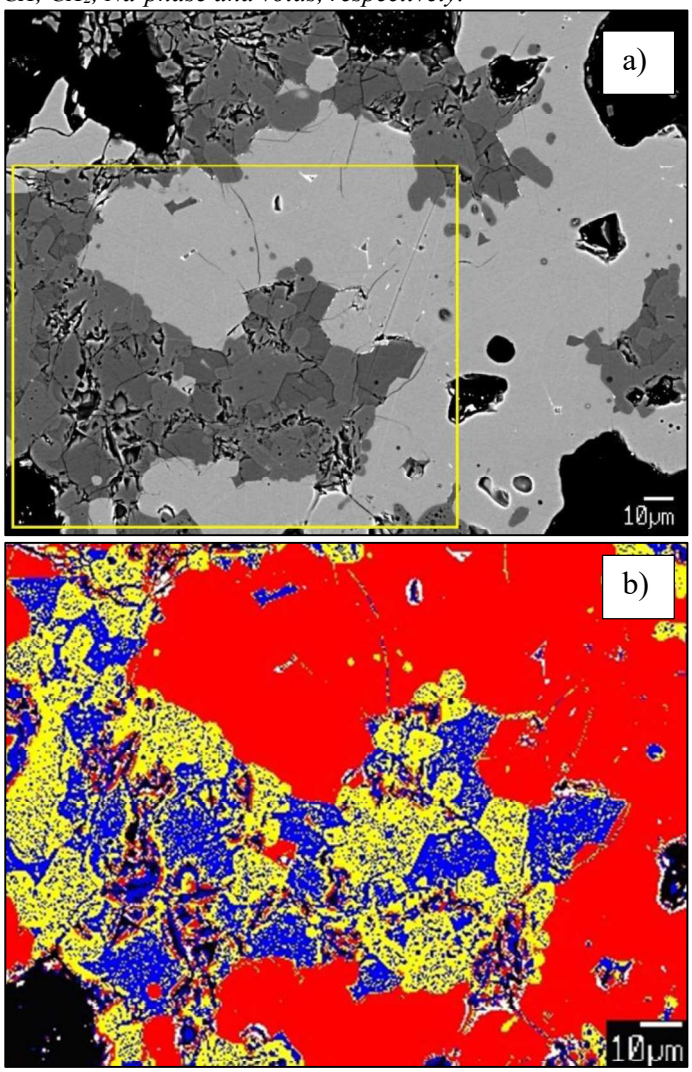


Hydration properties of *Na-phase* were studied by XRD at 3 and 8 hours, 1, 7, 14 days with a curing temperature of 18° C. Results highlighted a high-reactivity with water of $NCA_2$: (i) after 8 hours, *Na-phase* was partially dissolved and precipitated $CAH_{10}$ (ICDD 12-0408) [46], $AH_3$ (33-0018) [51], $C_3ACaCO_3{\cdot}11H_2O$ (ICDD 41-0219) [45] and minor $Ca_4Al_2O_6(CO_3)_{0.5}(OH){\cdot}11.5H_2O$ (ICDD 41-0221); (ii) after 1 day of hydration, $NCA_2$ completely reacted with water, moreover, the previous hydrated crystal phases continued to precipitate and gradually increased the degree of crystallinity; (iii) after 7 days, $C_3AH_6$ (ICDD 24-0217) [48] occurred as major crystal phase associated with $AH_3$, trace of $NaAlO_2{\cdot}5/4H_2O$ (ICDD 48-0289) [42] and $CAH_{10}$; (iv) after 14 days,

no more metastable hydrated crystal phases occurred, such as $CAH_{10}$ and/or $C_2AH_8$, only $NaAlO_2 \cdot 5/4H_2O$, $AH_3$ and $C_3AH_6$ were detected by XRD analysis.

***Fig. 13.*** *Diffraction patterns for Mix_NaP hydrated at 18° C at different curing time: a)14 days; b)7 days; c) 1 day; d) 8 hours; e) 3 hours. Principal peaks for $CAH_{10}$ (filled triangle), $C_3AH_6$ (open triangle), $AH_3$ (filled square), $NaAlO_2 \cdot 5/4H_2O$ (open square), $C_3ACaCO_3 \cdot 11H_2O$ (filled diamond), $Ca_4Al_2O_6(CO_3)_{0.5}(OH) \cdot 11.5H_2O$ (open diamond) and $Na_2CaAl_4O_8$ (filled star triangle) are reported.*

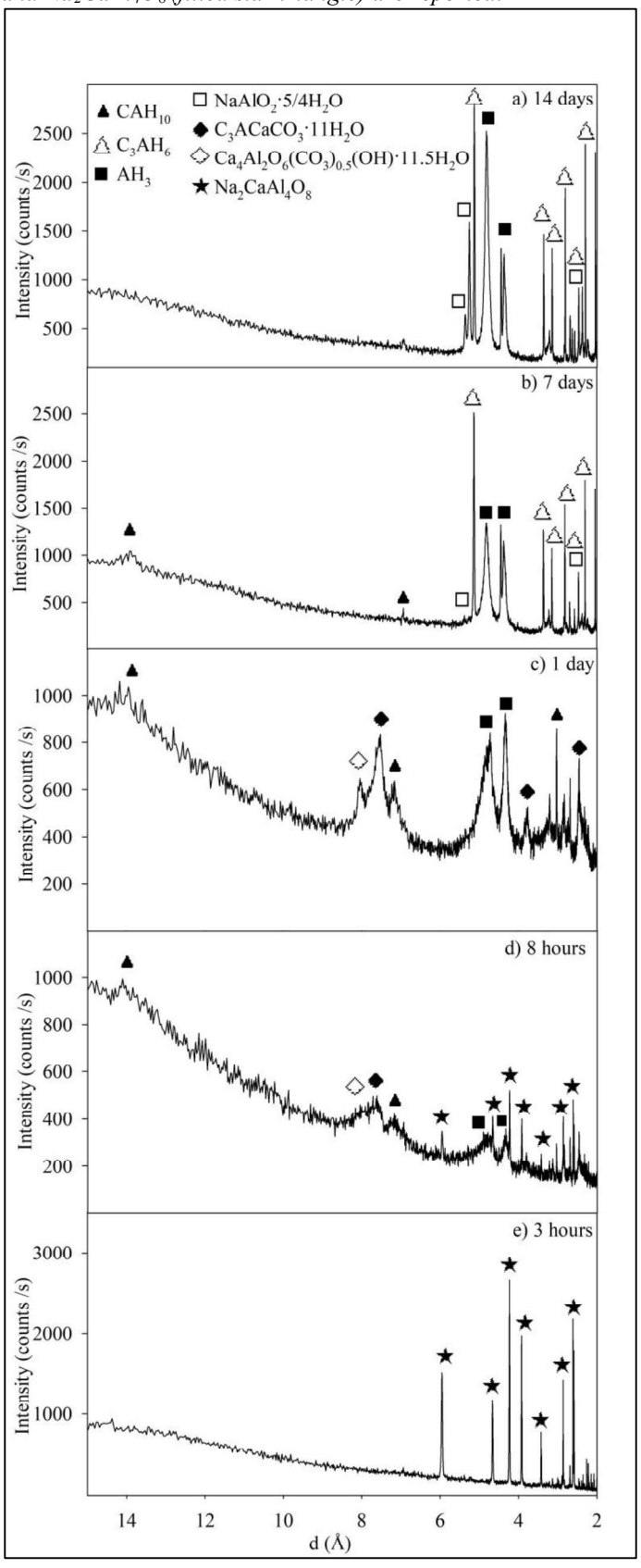

## 5. Discussion

The influence of the simultaneous presence of sodium and silicon as minor oxides on the final HACs mineralogy and microstructure is reported and discussed.

Results highlighted that at the clinkering temperature sodium and silicon do not favour the growth of secondary phases, i.e. gehlenite ($C_2AS$) and mayenite ($C_{12}A_7$), nor promote the crystallisation of an aluminate phase at the expense of the another one and/or the stabilisation of a certain polymorph, as usually reported in OPC chemistry [2,3,13,14,15,36].

The high variance in the HACs phase contents (i.e. $CA_2$ ranges from 21 to 44 in *HAC1_HNa* and *HAC2_HNa,* respectively) seems to be ascribed only to the different chemical composition of the starting raw meals rather than to the occurrence of minor elements. In particular, by comparing Tables 2 and 4 results it is clear that even small variations in the $CaO/Al_2O_3$ ratio in the starting raw meal induces large changes in the $CA/CA_2$ % wt. in the final HAC. Furthermore, form the SEM studies, the samples exhibit a similar microstructure in terms of crystal phase and size but show a different modal distribution of the two aluminate phases, thus supporting the XRPD data.

The unit cell values for CA suggest a limited degree of replacement by non-nominal elements in its crystal structure. The published volume cell of stoichiometric CA is 89.1811(1) $Å^3$ [27], while CA has values ranging from 89.13(3) to 89.20(4) $Å^3$ in all studied HACs, which falls withing the range of analytical errors. Notheless, chemical analysis on CA crystal revealed a negative correlation between $Na^{+}+Si^{4+}$ *vs* $Ca^{2+}+Al^{3+}$ (apfu), as reported in Fig. 10. These evidences suggest the occurrence of a limited ionic substitution in CA crystals as reported below:

$$^{IX}Ca^{2+} + {}^{IV}Al^{3+} \rightarrow {}^{IX}Na^{+} + {}^{IV}Si^{4+} \qquad \text{Eq. 3}$$

Sodium-rich HACs (*HACx_HNa* and *Mix_NaP*) are composed of CA, $CA_2$ and a sodium-rich phase ($Na_{1,9}Ca(Al_{3.9}Si_{0.1})O_8$), mentioned in this work as *Na-phase*); whereas sodium-depleted ones (*HACx_LNa*) are composed of only CA and $CA_2$. *Na-phase* was recognized from SEM/EMPA and high-resolution SXRPD analysis, while ordinary laboratory XRPD analysis was able to only

detected CA and $CA_2$. SXRPD analysis highlighted an unresolved Bragg peak with a low intensity and wide broadening at $d \cong 4.22$ Å, confirming the occurrence of an unknown phase (*Na-phase*) in an ordered crystalline structure.

The amorphous content evaluated by the internal standard method reveald a mean of 1.5% wt. and 3.5% wt. for sodium-rich and sodium-depleted HACs, respectively. The average $Na_2O$ underestimation of 0.4% wt. for sodium-rich industrial HACs, which was calculated from the difference between the bulk chemical composition (Table 2) and the recalculated ones using QXRPD values corrected from the amorhous content (Table 6), should be balances by the occurrence of around 2% wt. of *Na-phase*. Therefore, the average understimation of 0.2% wt. $SiO_2$ of sodium-rich industrial HACs could be partly balanced by the occurrence *Na-phase* and the remain content should be hosted in the amorphous phase, which is expected to be enriched in all elements that are not hosted in HACs crystal phases [44]. Image Analysis results (Table 5) confirmed the occurrence of around 2% vol. of *Na-phase* in sodium-rich HACs. Despite the evidence of low amorphous content by XRD results, no amorphous phase was detected during SEM/EMPA analysis.

The synthesis at laboratory scale of *Mix_NaP* and *Mix_CaNaAl* allow to gather additional information on the *Na-phase* and the effects of high-sodium content. The XRPD patterns of the synthetic samples confirmed the occurrence of a crystalline phase that has the same Bragg peaks of the *Na-phase* found in the industrial HACs. Moreover, *Na-phase* has same Bragg peaks of sodium-rich phase $N_2C_3A_5$ ($Na_4Ca_3Al_{10}O_{20}$) reported by Brownmiller and Bouge [34], and $NCA_2$ ($Na_2CaAl_4O_8$) by Verweij and Saris [22], therefore are all reporting the same crystal phase. Cell parameters and space group were identified by means of GSAS II [41] and EXPO [70] softwares indicating a $P2_12_12_1$ space group with $a$ = 7.2510 Å, $b$ = 10.4304 Å and $c$ = 10.4348 Å cell parameters. Yu et al. [43] reported the *Na-phase* has *P*222 space group with $a$ = 10.457 Å, $b$ = 7.265 Å and $c$ = 5.215 Å cell parameters, which are similar to our data but with three main differences occur: (i) $c$ vector is equal to our 1/2$b$ cell parameter, (ii) $a$ is equal to $b$ and viceversa ($a$

= *b*; *b* = *a*; *c* = 1/2*c*); the space group $P2_12_12_1$ has higher symmetry than *P*222 and systematic absences for all (*h*00), (0*k*0) and (00*l*) diffraction Bragg peaks equal to odd integer numbers [67] occur, which fits better XRD data. Verweij and Saris [22] reported the *Na-phase* as a tetragonal crystal structure with *a* = *b* = 10.4348 Å and *c* = 7.2539 Å cell parameters, nevertheless the similarities on cell parameters with our data, this choice should be rejected because in contrast with optical properties found by Brownmiller and Bogue [34] that recognized biaxial positive crystals: *Na-phase* should belong to orthorombic crystal system. Despite no crystal structure model for *Na-phase* is available, further investigation will be performed by Single Crystal X-ray Diffraction on suitable crystals found in the *Mix_NaP* solving its crystal structure. Some information on the crystal structure of *Na-phase* could be obtained from EMPA/SEM and petrological data [21,22,23,34,35,37,]. A complete solid solution between $NaAlO_2$ and *Na-phase*, therefore their crystal structures should be similar. EMPA analysis (Supplementary Materials Table 2) highlighted the occurrence of two ionic substitutions ($Ca^{2+} + \square \leftrightarrow 2\ Na^{+}$ and $Ca^{2+} + Al^{3+} \leftrightarrow Na^{+} + Si^{4+}$ and): the former supports the view that $NCA_2$ [21,22] and $N_2C_3A_5$ [23,25,34,37] represents the same crystal phase, with changes only in $Na_2O$ and CaO content, and the occurrence of not fully cationic sites; the replacement of $Al^{3+}$ by $Si^{4+}$, as commonly occurs in silicate minerals [1,36,39], suggests the occurrence of aluminium tehtrahedron $(AlO_4)^{5-}$. Therefore, *Na-phase* crystal structure should be a framework of aluminium tetrahedrons with channels/cages where $Ca^{2+}$ or $Na^{+}$ occur.

The occurrence of $CA_2$ and $NC_3A_5$ in *Mix_NaP* should be related only to very little chemical composition changes from stoichiometric values of $Na_2O{\cdot}CaO{\cdot}2Al_2O_3$ and/or to a limited loss in $Na_2O$, which should occur above 900 °C [34]. The phase assemblage $CA_2$-$NC_3A_5$-$NCA_2$ should have reached the thermodynamic stability considering the time left at 1200 °C (24 hours), nonetheless our phase assemblage does not occur in the reported isothermal section at 1200 °C (Fig. 3,4) [22,25]. Considering EMPA results, *Na-phase* revealed a slight increase in CaO and a decrease

in $Na_2O$ content in *Mix_CaNaAl* respect to industrial HACs: this result suggests the occurrence of a limited ionic substitution between $Na^+$ by $Ca^{2+}$ following the exchange $Ca^{2+} + \square \leftrightarrow 2\ Na^+$.

Hydration of *Na-phase* at 18° C from 3 hours to 14 days highlighted a rapid reactivity with water: *Na-phase* was completely dissolved in water and started to precipitate $C_3AH_6$ just after 1 day; after 14 days the phase assemblage is composed of $C_3AH_6$, $AH_3$ and $NaAlO_2 \cdot 5/4H_2O$. The hydration reactions of *Na-phase* seems to be similar to those one reported for calcium aluminate phases (CA and $CA_2$) at low temperature [1,46] without the precipitation of $C_2AH_8$: $CAH_{10}$ firstly appears and is rapidly converted to a more stable mineral assemblage composed of $C_3AH_6$ and $AH_3$ [1]. No sodium carbonates were found, so $NaAlO_2 \cdot 5/4H_2O$ represents the only sodium-rich crystal phase after 14 days of hydration. Therefore, the occurrence of *Na-phase* in industrial HACs (*HACx_HNa*) during the hydration stage could enhance the hydraulic reactivity and increases the conversion rate of metastable hydrates ($CAH_{10}$ and $C_2AH_8$) to the more stable mineral assemblage dominated by hydrogarnet ($C_3AH_6$) and gibbsite ($AH_3$). Currel et al. [44] reported that sodium respresents an acceleration additive in HACs during hydration.

SEM analysis confirmed a microstructural similarity among HACs and laboratory sample (*Mix_CaNaAl*) where *Na-phase* appeared as crystals with a prismatic habit and a grain size ranging from 10 to 20 µm. The mineral assemblage CA-$CA_2$-$NCA_2$ observed in studied HACs appeared in thermodynamic equilibrium without the occurrence of a detectable amorphous phase. Nevertheless, our data are in disagreement with Brownmiller and Bogue [34] data, which reported a melting point of 1465° C for HACs composition: the melting of CA-$CA_2$-$NCA_2$ should need more than 1 hour of heating to occur, even if the heating temperature exceeds 1465 °C.

*Mix_NaP* is composed of mainly $NCA_2$ (*Na-phase*) with minor $NC_3A_8$ ($Na_2Ca_3Al_{16}O_{28}$) and $CA_2$ after 24 hours of heating at 1200±15 °C. The crystal phase $NC_3A_8$ was firstly observed by Verweij and Saris [22] and does not appear on the liquidus surface, as reported Brownmiller and Bogue [34], therefore $NC_3A_8$ should decompose at higher temperature (> 1200 °C). The mineral assemblage $CA_2$-$NCA_2$-$NC_3A_8$ does not appear in Verweij and Saris [22] isothermal section at 1200 °C and

*Mix_NaP* falls within in the CA-$NCA_2$-$NCA_3$ stability field: this difference in phase assemblage should be related to a slightly higher heating temperature in our experiment respected to bibliographical ones [22], leading the appearance of the $NCA_2$-$CA_2$ *tie-line* instead of CA-$NC_3A_8$ one and thus formation of $CA_2$-$NCA_2$-$NCA_3$ stability field.

**Conclusion**

Our study reports the effect of sodium and silicon, both separately and combined, in HACs, which they represent most common impurities in ordinary and innovative HACs raw materials, such as synthetic alumina and Al-rich wastes, respectively. Adding a limited amount of silicon (up to 0.5% wt.) combined with traces of $Na_2O$ (up to 0.10% wt.) in HACs no significant variation related to the mineral assemblage and chemical composition of crystal phases is observed, despite should occurs gehlenite as silicon-bearing phase. Whereas, adding sodium, both alone or combined with silicon, resulted in the crystallisation of a sodium-rich crystal phase (*Na-phase*, $Na_{2-x}Ca_{1-x}Al_{4-x}Si_xO_8$ with $x < 0.11$), which hosts most of the $Na_2O$ and $SiO_2$ content and other minor elements, due to the limited ionic substitution observed in CA and $CA_2$ for these elements. Despite its occurrence no single crystals were available for crystal structure solution by Single Crystal X-ray Diffraction: further diffractometric investigations will be performed on this crystal phase to resolve its crystal structure.

Even if the low content of impurities in CA and $CA_2$ crystals, punctual chemical analysis revealed that CA can host more sodium and silicon than $CA_2$ through a coupled ionic substitution $^{IX}Ca^{2+} + {}^{IV}Al^{3+} \rightarrow {}^{IX}Na^{+} + {}^{IV}Si^{4+}$, thanks to the occurrence of nine-fold cationic site in CA, where could be hosted $Na^{+}$.

The absence of amorphous phase with the composition predicted by the ternary phase diagram CaO-$Al_2O_3$-$Na_2O$ [25] and the lack of typical microstructural features related to partial melted material, suggest that thermodynamic equilibrium is not reached, as usually occur in OPC

manufacture. This suggests that the achievement of the thermodynamic equilibrium in HAC manufacturing requires an increase of the heating time of the raw meal in the rotary kiln than that actually used in HACs manufacture.

Due to the high resolution of Synchrotron X-ray Powder Diffraction, a deep study on mineral assemblage on HACs was performed, highlighting that no $C_2AS$ for HACs composition occurred: sodium can inhibit the crystallisation of gehlenite, which represents the most commonly unwanted minor crystal phases in HACs, occurring also at low silicon content [1]. Gehlenite strongly influences refractory properties dramatically reducing the melting point and lowering the hydration properties; therefore its absence improves HACs properties [1,2,3,4].

In conclusion, sodium and silicon, which commonly occur as minor oxides in natural and/or alternative raw materials used in HACs manufacture, result in the occurrence of *Na*-phase which does not significantly change the melting point during heating process and has a fast water reactivity. These evidences could be the starting point for the development of a new HACs type (*Na-phase-rich* HACs) that has the chance to handle the shortage of suitable bauxite and its high energy demanding treatment by re-using of Al-rich wastes as raw materials, which nowadays represents a critical environmental problem. Nevertheless, further investigations on the crystal structure of *Na-phase* and tests on the hydration and mechanical properties on *Na-phase-rich* HACs pastes at early and long hydration time are needed [1,2,3,4].

## Acknowledgments

The authors acknowledge the support of the Italian Ministry of Education (MIUR) through the project "PRIN2017—Mineral reactivity, a key to understand large-scale processes" for the XRPD and EMPA analyses. The authors would like to thank Andrea Risplendente, who performed SEM and EMPA analysis.

# Reference


[1] H. Pöllmann, Calcium Aluminate Cements – Raw Materials, Differences, Hydration and Properties, Reviews in Mineralogy and Geochemistry 74 (2012) 1 82, https://doi.org/10.2138/rmg.2012.74.1

[2] P.C. Hewlett, Lea's Chemistry of cement and concrete, 4th edition, Elsevier Science & Technology Books, 2004

[3] H. F.W. Taylor, Cement chemistry, Thomas Telford Publishing, 1997

[4] W. Kurdowski, Cement and concrete chemistry, Springer, 2014

[5] M.C.G. Juenger, F. Winnefeld, J.L. Provis, J.H. Ideker, Advances in alternative cementitious binders, Cement and Concrete Research 41 (2011) 1232-1243, https://doi.org/10.1016/j.cemconres.2010.11.012.

[6] I.N. Chakraborty, A.K. Chattopadhyay, Manufacture of High Alumina Cement: An Indian Experience, in International conference, Calcium aluminate cements (2001) 25-33

[7] R. Bolger, Non-refractory bauxite, Industrial Minerals (1997) 21-29

[8] M.F. Zawrah, N.M. Khalil, Utilisation of Egyptian industrial waste material in manufacture of refractory cement, British Ceramic Transactions 101 (2002) 225-228, https://doi.org/101:5, 225-228

[9] S.A.S. El-Hemaly, N.M. Khalil, L.G. Girgis, Refractory castables based on barium aluminate cements, British Ceramic Transactions 103 (2003) 169-174, https://doi.org/10.1179/096797803225004954

[10] E.M.M. Ewais, N.M. Khalil, M.S. Amin, Y.M.Z. Ahmed, M.A. Barakat, Utilization of aluminum sludge and aluminum slag (dross) for the manufacture of calcium aluminate cement, Ceramics International 35 (2009) 3381-3388, https://doi.org/10.1016/j.ceramint.2009.06.008

[11] De la Torre Á.G., Cuberos A.J.M., Álvarez-Pinazo G., Cuesta A., Aranda M.A.G., In situ powder diffraction study of belite sulfoaluminate clinkering, J. Synchrotron Rad. 18 (2011) 506-514. https://doi.org/10.1107/S0909049511005796

[12] K. Morsli, A.G. De la Torre, M. Zahir, M.A.G. Aranda, Mineralogical phase analysis of alkali and sulfate bearing belite rich laboratory clinker, Cem. Concr. Res. 37 (2007) 639-646. https://doi.org/10.1016/j.cemconres.2007.01.012

[13] Skibsted J., Sevelsted T.F., Poulsen S.L., Tran T.T., Studies on guest-ion incorporation in Portland cement — Part 1, ZKG Int. 66 (2013a) 66.

[14] Skibsted J., Sevelsted T.F., Poulsen S.L., Tran T.T., Studies on guest-ion incorporation in Portland cement — Part 2, ZKG Int. 66 (2013b) 46.

[15] Bhatty J. I., Role of Minor Elements in Cement Manufacture and Use, Portland Cement Association, 1995. https://trid.trb.org/view/461431

[16] M. Murat, F. Sorrentino, Effect of large additions of Cd, Pb, Cr, Zn, to cement raw meal on the composition and the properties of the clinker and the cement, Cement and Concrete Research 26 (1996) 377-385, https://doi.org/10.1016/S0008-8846(96)85025-3

[17] N.M. Khalil, S.AS. El-Hemaly, L. Girgis, Aluminous Cements Containing MA Spinel from Egyptian Dolomite. Ceramics International. 27 (2001) 865-873, https://doi.org/10.1016/S0272-8842(01)00042-6

[18] E. Dourdounis, V. Stivanakis, G.N. Angelopoulos, E. Chaniotakis, E. Frogoudakis, D. Papanastasiou, D.C. Papamantellos, High-alumina cement production from FeNi-ERF slag, limestone and diasporic bauxite, Cement and Concrete Research 34 (2004) 941-947, https://doi.org/10.1016/j.cemconres.2003.11.004

[19] H. Pöllmann, R. Obeste-Padtberg, Manganese in high alumina cement (HAC), in International conference, Calcium aluminate cements (2001) 139-149.

[20] Andrew R. Hind, Suresh K. Bhargava, Stephen C. Grocott, The surface chemistry of Bayer process solids: a review, Colloids and Surfaces A: Physicochemical and Engineering Aspects 146 (1999) 359-374. https://doi.org/10.1016/S0927-7757(98)00798-5
[21] C. Ostrowski, J. Żelazny, Solid Solutions of Calcium Aluminates $C_3A$, $C_{12}A_7$ and CA with Sodium Oxide, Journal of Thermal Analysis and Calorimetry 75 (2004) 867-885. https://doi.org/10.1023/B:JTAN.0000027182.40442.fe
[22] H. Verweij, C.M.P.M Saris, Phase Formation in the System $Na_2O{\cdot}Al_2O_3$-$CaO{\cdot}A1_2O_3$-$Al_2O_3$ at 1200°C in Air, Journal of the American Ceramic Society 69 (1986). https://doi.org/10.1111/j.1151-2916.1986.tb04708.x
[23] H. Yu, X. Pan, B. Wang, W. Zhang, H. Sun, S. Bi, Effect of $Na_2O$ on formation of calcium aluminates in CaO–$Al_2O_3$–$SiO_2$ system. Transactions of Nonferrous Metals Society of China 22 (2012) 3108–3112. https://doi.org/10.1016/S1003-6326(11)61578-1.
[24] J. Alex, L. Vandeperre, W.E. Lee, B. Touzo, C. Parr, Effect of Sodium on Microstructures and Thermoelastic Properties of Calcium Aluminate Cement–Bonded Refractories. J. Am. Ceram. Soc. 99 (2016) 1079-1085. https://doi.org/10.1111/jace.14046
[25] Bale, C.W., E. Bélisle, P. Chartrand, S. Decterov, G. Eriksson, A. Gheribi, K. Hack, I.-H. Jung, Y.-B. Kang, and J. Melançon, FactSage thermochemical software and databases, 2010–2016. Calphad 54 (2016), 35-53. https://doi.org/10.1016/S0364-5916(02)00035-4
[26] L.D. Bish and S.A. Howard, Quantitative phase analysis using the Rietveld method, J. Appl. Cryst. 21 (1988) 86-91. https://doi.org/10.1107/S0021889887009415
[27] R.W. Cheary and Coelho A. A Fundamental Parameters Approach to X-ray Line-Profile Fitting. J. Appl. Cryst. 25 (1992) 109-121. https://doi.org/10.1107/S0021889891010804
[28] A. A. Coelho, Technical Reference Topas-Academic Version 6, Bruker-AXS (2016) http://www.topas-academic.net/Technical_Reference.pdf
[29] Palacios L, De La Torre A G, Bruque S, García-Muñoz J L, García-Granda S, Sheptyakov D and Aranda M A. Crystal structures and in-situ formation study of mayenite electrides. Inorg Chem., 46 (2007) 4167-76. https://doi.org/10.1021/ic0700497
[30] Efremov V A, Gutnikov S I, Kartashov A A and Lazoryak. Average Grossite Crystal Structure. Personal Communication to COD, 2012.
[31] Pouchou J L and Pichoir F. Microbeam Analysis. D. E. Newbury edition San Francisco Press ,1988.
[32] Hill R J and Fischer R X. Profile agreement indices in Rietvled and pattern fitting analysis. J. Appl. Cryst. 23 (1990) 462-468. https://doi.org/10.1107/S0021889890006094
[33] F. Guirando, S. Galì, Quantitative Rietveld analysis of CAC clinker phases using synchrotron radiation, Cem. Concr. Res. 36 (2006), 2021-2032. https://doi.org/10.1016/j.cemconres.2006.05.019
[34] L. T. Brownmiller and R. H. Bogue, System CaO-$Na_2O$-$Al_2O_3$, J . Res. Natl. Bur. Stand. (U.S.) 8 (1932) 289-307.
[35] Y.P. Tian, X.L. Pan, H.Y. Yu, G.F. Tu, Formation mechanism and crystal simulation of $Na_2O$-doped calcium aluminate compounds. Trans. Nonferrous Met. Soc. China 26 (2016) 849−858. https://doi.org/10.1016/S1003-6326(16)64176-6
[36] M. Segata, N. Marinoni, M. Galimberti, M. Marchi, M. Cantaluppi, A. Pavese, À. G. De la Torre, The effects of MgO, $Na_2O$ and $SO_3$ on industrial clinkering process: phase composition, polymorphism, microstructure and hydration, using a multidisciplinary approach, Materials Characterization 155 (2019) 109809-109819. https://doi.org/10.1016/j.matchar.2019.109809
[37] H.Y. Yu, X.L. Pan, Y.P. Tian, G.F. Tu. Mineral transition and formation mechanism of calcium aluminate compounds in CaO-$Al_2O_3$-$Na_2O$ system during high-temperature sintering, Int. J. Miner. Metall. Mater (2019) 924-932. https://doi.org/10.1007/s12613-019-1951-1
[38] R.D. Shannon, Revised effective ionic radii and systematic studies of interatomie distances in halides and chaleogenides, Acta Cryst. A32 (1976) 751-767. https://doi.org/10.1107/S0567739476001551

[39] F. Guirando, S. Gali, S. Chinchòn, Quantitative Rietveld analysis of aluminous cement clinker phases, Cem. Conc Res. 30 (2000) 1023-1029. https://doi.org/10.1016/S0008-8846(00)00289-1
[40] J. Bensted, P. Barnes, Structure and Performace of Cements 2nd Edition, CRC Press, 2001.
[41] B.H. Toby, R.B. Von Dreele, GSAS-II: the genesis of a modern open-source all purpose crystallography software package, Journal of Applied Crystallography 46 (2007) 544-549. https://doi:10.1107/S0021889813003531
[42] J.A. Kaduk, S. Pei, The crystal structure of hydrated sodium aluminate, $NaAlO_2 \cdot 5/4H_2O$, and its dehydration product, Journal of solid state chemistry, 155 (1995) 126-139. https://doi.org/10.1006/jssc.1995.1111
[43] B.R. Currell, R. Grzeskowlak, H.G. Mldgley, J.R. Parsonage, the acceleration and retardation of set high allnina cement by additives, Cem. Concr. Res. , 7 (1987) 420-432,. https://doi.org/10.1016/0008-8846(87)90006-8.
[44] M. Cantaluppi, F. Cella, K. Kagan, N. Marinoni, F. Cámara, An investigation of the chemical distribution of minor elements in high alumina cements by a multidisciplinary approach, in International conference, Calcium aluminate cements, (2020). ISBN-10 1849954763, ISBN-13 978-1849954761
[45] M. François, G. Renaudin, O. Evrard, A cementitious compound with composition $3CaO.Al_2O_3$-$CaCO_3.11H_2O$, Acta Crystallogr. Sect. C Cryst. Struct. Commun. (1998). https://doi.org/10.1107/S0108270198004223.
[46] F. Guirado, S. Galí, S. Chinchón, J. Rius, Crystal Structure Solution of Hydrated High-Alumina Cement from X-ray Powder Diffraction Data, Angew. Chemie - Int. Ed. (1998). https://doi.org/10.1002/(sici)1521-3773(19980202)37:1/2<72::aid-anie72>3.0.co;2-8.
[47] M. Schreyer, L. Guo, S. Thirunahari, F. Gao, M. Garland, Simultaneous determination of several crystal structures from powder mixtures: The combination of powder X-ray diffraction, band-target entropy minimization and Rietveld methods, J. Appl. Crystallogr. (2014). https://doi.org/10.1107/S1600576714003379.
[48] C. Cohen-Addad, P. Ducros, A. Durif, E.F. Bertaut, A. Delapalme, Détermination de la position des atomes d'hydrogène dans l'hydrogrinat Al2O3, 3CaO, 6H2O par résonance magnétique nucléaire et diffraction neutronique, J. Phys. (1964). https://doi.org/10.1051/jphys:01964002505047800.
[49] A. Altomare, N. Corriero, C. Cuocci, A. Falcicchio, A. Moliterni, R. Rizzi, EXPO software for solving crystal structures by powder diffraction data: Methods and application, Cryst. Res. Technol. (2015). https://doi.org/10.1002/crat.201500024.
[50] A.D. Elliot, Structure of pyrrhotite 5C (Fe9S10), Acta Crystallogr. Sect. B Struct. Sci. (2010). https://doi.org/10.1107/S0108768110011845.
[51] K. Komatsu, T. Kuribayashi, Y. Kudoh, H. Kagi, Crystal structures of high-pressure phases in the alumina-water system: I. Single crystal X-ray diffraction and molecular dynamics simulation of η-Al(OH)3, Zeitschrift Fur Krist. (2007). https://doi.org/10.1524/zkri.2007.222.1.1.
[52] R.T. Downs, M. Hall-Wallace, The American Mineralogist crystal structure database, Am. Mineral. (2003). https://doi.org/10.5860/choice.43sup-0302.
[53] S. Graulis, D. Chateigner, R.T. Downs, A.F.T. Yokochi, M. Quirós, L. Lutterotti, E. Manakova, J. Butkus, P. Moeck, A. Le Bail, Crystallography Open Database - An open-access collection of crystal structures, J. Appl. Crystallogr. (2009). https://doi.org/10.1107/S0021889809016690.
[54] S. Gražulis, A. Daškevič, A. Merkys, D. Chateigner, L. Lutterotti, M. Quirós, N.R. Serebryanaya, P. Moeck, R.T. Downs, A. Le Bail, Crystallography Open Database (COD): An open-access collection of crystal structures and platform for world-wide collaboration, Nucleic Acids Res. (2012). https://doi.org/10.1093/nar/gkr900.
[55] S. Gražulis, A. Merkys, A. Vaitkus, M. Okulič-Kazarinas, Computing stoichiometric molecular composition from crystal structures, J. Appl. Crystallogr. (2015). https://doi.org/10.1107/S1600576714025904.

[56] A. Merkys, A. Vaitkus, J. Butkus, M. Okulič-Kazarinas, V. Kairys, S. Gražulis, COD::CIF::Parser: An error-correcting CIF parser for the Perl language, J. Appl. Crystallogr. (2016). https://doi.org/10.1107/S1600576715022396.
[57] M. Quirós, S. Gražulis, S. Girdzijauskaitė, A. Merkys, A. Vaitkus, Using SMILES strings for the description of chemical connectivity in the Crystallography Open Database, J. Cheminform. (2018). https://doi.org/10.1186/s13321-018-0279-6.
[60] https://www.crct.polymtl.ca/fact/pdweb.php
[61] J.-L. Hodeau, P. Bordet, M. Anne, A. Prat, A.N. Fitch, E. Dooryhee, G. Vaughan, A.K. Freund, Nine-crystal multianalyzer stage for high-resolution powder diffraction between 6 keV and 40 keV, in: Cryst. Multilayer Opt. (1998). https://doi.org/10.1117/12.332525.
[62] J.Wright, G.B.M. Vaughan, A. Fitch, Merging data from a multi-detector continuous powder diffraction system, Commission on Crystal Computing 1 (2003) 92.
[63] D. Siderius, NIST Standard Reference Simulation Website - SRD 173 (Version 1.0.0) [Data set], National Institute of Standards and Technology (2017). https://doi.org/10.18434/T4M88Q
[64] A.G. De La Torre, S. Bruque, M.A.G. Aranda, Rietveld quantitative amorphous content analysis, J. Appl. Crystallogr. (2001). https://doi.org/10.1107/S0021889801002485.
[65] S. Sengo, P. Romano Triguero, E. Zinngrebe, F. Mensonides, Tracing the Origin of Non-ferrous Oxides in Lamination Defects on Hot-Rolled Coils: Mold Slag Entrainment vs Submerged Entry Nozzle Reaction Products, Metall. Mater. Trans. B Process Metall. Mater. Process. Sci. (2017). https://doi.org/10.1007/s11663-017-0928-6.
[66] S. Rashid, P. Barnes, X. Turrillas, The rapid conversion of calcium aluminate cement hydrates, as revealed by synchrotron energy-dispersive diffraction, Adv. Cem. Res. (1992). https://doi.org/10.1680/adcr.1992.4.14.61.
[67] C. Giacovazzo, C. Giacovazzo, Fundamentals of crystallography, in: Phasing Crystallogr., 2013. https://doi.org/10.1093/oso/9780199686995.003.0006.
[68] M.I. Aroyo, J.M. Perez-Mato, C. Capillas, E. Kroumova, S. Ivantchev, G. Madariaga, A. Kirov, H. Wondratschek, Bilbao Crystallographic Server: I. Databases and crystallographic computing programs, in: Zeitschrift Fur Krist., 2006. https://doi.org/10.1524/zkri.2006.221.1.15.
[69] V. Kahlenberg, On the Al/Fe substitution in iron doped monocalcium aluminate - the crystal structure of CaAl1.8Fe0.2O4, Eur. J. Mineral. (2001). https://doi.org/10.1127/0935-1221/01/0013-0403.
[70] X. Cong, R.J. Kirkpatrick, Hydration of Calcium Aluminate Cements: A Solid- State $^{27}$Al NMR Study, J. Am. Ceram. Soc. (1993). https://doi.org/10.1111/j.1151-2916.1993.tb03799.x.
[71] Souza, M. T., Simão, L., Montedo, O. R. K., Raupp Pereira, F., & de Oliveira, A. P. N. (2019). Aluminum anodizing waste and its uses: An overview of potential applications and market opportunities. *Waste Management*. https://doi.org/10.1016/j.wasman.2018.12.003
[72] Ewais, E. M. M., Khalil, N. M., Amin, M. S., Ahmed, Y. M. Z., & Barakat, M. A. (2009). Utilization of aluminum sludge and aluminum slag (dross) for the manufacture of calcium aluminate cement. *Ceramics International*. https://doi.org/10.1016/j.ceramint.2009.06.008
[73] Qingsheng, L., Chunming, Z., Hui, F., & Jilai, X. (2011). High Purity Alumina Powders Extracted from Aluminum Dross by the Calcining-Leaching Process. In *Light Metals 2011*. https://doi.org/10.1002/9781118061992.ch34
[74] Krivoborodov, Y., & Samchenko, S. (2019). Synthesis of high alumina cement based on metallurgy wastes. *IOP Conference Series: Materials Science and Engineering*. https://doi.org/10.1088/1757-899X/687/2/022034
[75] Das, B. R., Dash, B., Tripathy, B. C., Bhattacharya, I. N., & Das, S. C. (2007). Production of η-alumina from waste aluminium dross. *Minerals Engineering*. https://doi.org/10.1016/j.mineng.2006.09.002

**Declaration of interests**

☒ The authors declare that they have no known competing financial interests or personal relationships that could have appeared to influence the work reported in this paper.

☐The authors declare the following financial interests/personal relationships which may be considered as potential competing interests:

**CrediT Author Statement**

All authors contributed to the ideas and evolution of aims of the project, methodology, supervision during writing and providing study materials (reagents, laboratory samples and instrumentations).

Mainly the first author, Prof. N. Marinoni and Prof. F. Cámara were involved in the reproducibility of results, performing the experiments, data curation and writing the manuscript.

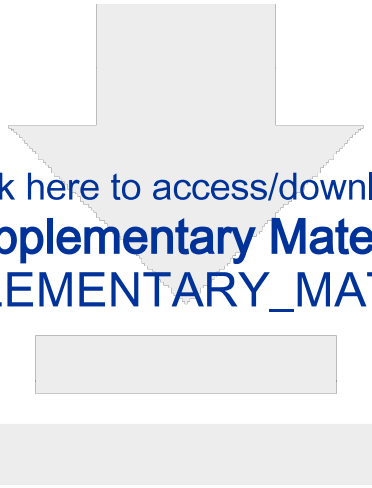

Click here to access/download

**Supplementary Material**

09_03_SUPPLEMENTARY_MATERIALS.docx